A Coupled CFD-DEM investigation of suffusion of gap graded soil: coupling effect of confining pressure and fines content

Yajing Liu[a,b], Lizhong Wang[a,b], Yi Hong[*a,b], Jidong Zhao [c], Zhen-yu Yin [d]

a. Key Laboratory of Offshore Geotechnics and Material of Zhejiang Province, Hangzhou, China
b. College of Civil Engineering and Architecture, Zhejiang University, Hangzhou, China
c. Department of Civil and Environmental Engineering, The Hong Kong University of Science and Technology, Clear Water Bay, Kowloon, Hong Kong, China
d. Department of Civil and Environmental Engineering, The Hong Kong Polytechnic University, Kowloon, Hong Kong, China
* Corresponding author, Postal address: Anzhong Building, Zijingang Campus, Zhejiang University, Hangzhou, China; Email: yi_hong@zju.edu.cn

Abstract: Suffusion involves fine particles migration within the matrix of coarse fraction under seepage flow, which usually occurs in the gap-graded material of dams and levees. Key factors controlling the soil erodibility include confining pressure (p') and fines content (F_c), of which the coupling effect on suffusion still remains contradictory, as concluded from different studies considering narrow scope of these factors. For this reason, a systematical numerical simulation that considers a relative wide range of p' and F_c was performed with the coupled discrete element method (DEM) and computational fluid dynamics (CFD) approach. Two distinct macro-responses of soil suffusion to p' was revealed, i.e., for a given hydraulic gradient i=2, an increase in p' intensifies the suffusion of soil with fines overfilling the voids (e.g., F_c =35%), but have negligible effects on the suffusion of gap-graded soil containing fines underfilling the voids (e.g., F_c =20%). The micromechanical analyses, including force chain buckling and strain energy release, reveal that when the fines overfilled the voids between coarse particles (e.g., F_c =35%) and participated heavily in load-bearing,

the erosion of fines under high i could cause the collapse of the original force transmission structure. The release of higher strain energy within samples under higher p' accelerated particle movement and intensified suffusion. Conversely, in the case where the fines underfilled the voids between coarse particles (e.g., F_c=20%), the selective erosion of fines had little influence on the force network. High p' in this case prevented suffusion.

Key words: suffusion, CFD-DEM, confining pressure, fines content, force chain buckling, strain energy

1. Introduction

Suffusion usually occurs within gap-graded coarse material, where the instability and loss of fines are triggered under the action of seepage as shown in Fig. 1(a). It is indisputable that the significant changes of hydraulic and mechanical behavior of the soil induced by suffusion are the cause of many unfavorable evolutions, which may lead to failure. Previous experimental and theoretical studies on suffusion have revealed that the erodibility of gap-graded soil is significantly influenced by confining pressure (p') and fines content (F_c) (Tomlinson and Vaid, 2000; Papamichos, 2001; Bendahmane et al, 2008; Richards and Reddy, 2010; Li and Fannin, 2012; Luo et al., 2013; Chang and Zhang, 2013; Shire and O'Sullivan, 2013; Shire et al., 2014; Ke and Takahashi, 2014; Wang et al., 2014; Liang et al., 2017; Yang et al., 2019; Yang et al., 2020). It was concluded from some studies that a higher confining pressure (p') may help to prevent

the occurrence of suffusion, due to the resulted increase in the inter-particle contact force and particle connectivity (Shire and O'Sullivan, 2013; Shire et al., 2014; Kawano et al., 2018; Hu et al., 2019). Conversely, it was revealed from other studies that an increasing confining pressure could have intensifies the suffusion (e.g., more fines loss) of a gap-graded soil (Tomlinson and Vaid, 2000; Papamichos, 2001; Bendahmane et al, 2008; Chang, 2013). The contradictory observations on the influences of p' probably are resulted from the narrow scope of the influential factors (i.e., p' and F_c) considered in each study. For example, most experiments revealing that suppressed erodability by higher p' were generally carried out based on gap-graded soil with relatively low F_c (fines underfilling the voids of coarse grains) (Wang et al., 2014; Liang et al., 2017). While the tests showing intensified erodibility by higher p' were mainly performed based on gap-graded soil with relatively high F_c (fines overfilling the voids of coarse grains) (Papamichos, 2001; Bendahmane et al, 2008; Chang, 2013).

Currently, numerical experiments of such problems were mainly carried out by the coupled computational fluid dynamics (CFD) and discrete element method (DEM) technique. Researchers utilized a coarse-grid CFDDEM, in which a fluid grid accommodates about 10 particles, to investigate the microscopic particle erosion and transport process within gap-graded soils (Kawano et al., 2018; Hu et al., 2019; Xiong et al., 2020). Some researchers adopted a fine-grid CFDDEM, where the fluid grid is much smaller than a particle and their interactions are directly computed by the commonly-used immersed boundary method, to study fluid-particle systems (Jin et al.,

2012). Recently, a coupled lattice Boltzmann method (LBM), which is an advanced high-resolution CFD solver for fluid flow, and DEM approach has been attracting substantial attention of researchers in geomechanics. Its application in the erosion and subsequent migration of fine particles was first reported by Wang et al., (2017). An advanced algorithm of LBMDEM can be found in the literature (Wang et al., 2019).

In view of the aforementioned issues, this study aims to obtain a better understanding on the coupling effect of F_c and p' on the erodibility of gap-graded sand samples, and to shed micromechanical insights into the phenomenon. Given the computational power and efficiency of current computers, this is achieved by performing coupled discrete element method (DEM) and computational fluid dynamics (CFD) simulations on the suffusion of gap-graded sand samples, with consideration of a broad range of F_c and p', using the coarse-grid CFDDEM technique. The simulated macro-response (including the eroded particles mass and samples deformation) were presented, showing distinct roles played by p' at different F_c, i.e., suppressed erodibility by increasing p' at relatively low F_c, and intensified erodibility by increasing p' at relatively higher F_c. These distinct responses are interpreted from the micromechanical perspectives, including evolving of loading bearing, force chain buckling and strain energy. The shear stress (q) and soil density are not considered in this study. Both of them also have significant effects on suffusion (Chang and Zhang, 2013; Luo et al., 2019; Wauiter, 2019; Israr and Indraratna. 2019), which could be analyzed in future work.

2. Coupled CFD-DEM method

The coupled CFD-DEM method used in this study included three types of formulations: the discrete element method (DEM), computational fluid dynamics (CFD) and the CFD-DEM coupling formulation. The DEM code LIGGGHTS is responsible for simulating massive dispersed particle bodies through Newton's law. The CFD code OpenFOAM is a common tool for simulating hydrodynamic processes through solving the continuity and Navier-Stokes equations. In this study, the particle-fluid interaction, including the drag force, pressure gradient force and viscous force, is calculated by the CFDEM program developed by Goniva et al. (2012) and Kloss et al. (2012). Governing equations for DEM, CFD, and coupling procedures are given in the following sub-sections.

2.1 Governing equations for DEM

DEM is a widely used approach for simulating the behavior of massive dispersed particles based on Newton's second law of motion. At any time t, the equation governing the translational and rotational motion of particle i is

$$\begin{cases} m_i \dfrac{d\mathbf{U}_i}{dt} = \sum_{j=1}^{n_i^c} \mathbf{F}_{ij}^c + \mathbf{F}_i^f \\ I_i \dfrac{d\boldsymbol{\omega}_i}{dt} = \sum_{j=1}^{n_i^c} \mathbf{M}_{ij} \end{cases} \tag{1}$$

where m_i and I_i denote the mass and moment of inertia of particle i, respectively. $\mathbf{U}_i$ and $\boldsymbol{\omega}_i$ are the transitional and angular velocities of particle i, respectively. The forces involved include the contact force and torque acting on particle i by particle j (i.e., $\mathbf{F}_{ij}^c$

and $\mathbf{M}_{ij}$), as well as the particle-fluid interaction force acting on particle *i* (i.e., $\mathbf{F}_i^f$). n_i^c is the number of contacts of the particle *i*.

In the DEM code, the Hertzian contact law (Mindlin and Deresiewicz, 1953; Renzo and Maio, 2004) is employed in conjunction with Coulomb's friction law to describe the inter-particle contact behavior. The contact behavior is governed by the normal and tangential stiffness at the contacts (i.e., k_t and k_n, respectively), as formulated below:

$$k_n = \frac{4}{3} E^* \sqrt{R^* \delta_n} \tag{2a}$$

$$k_t = 8G^* \sqrt{R^* \delta_n} \tag{2b}$$

where E^* and G^* are the equivalent elastic and shear modulus, respectively. R^* is the equivalent radius for two contacting particles. As shown in Eqs. 2(a) and (2b), both of the contact normal and tangential stiffness are functions of elastic moduli (E^* and G^*), a particle-radius related parameter (R^*) and inter-particle overlap (δ_n). The term E^*, G^* and R^* can be further expressed as:

$$\frac{1}{E^*} = \frac{1-v_i^2}{E_i} + \frac{1-v_j^2}{E_j} \tag{3a}$$

$$\frac{1}{G^*} = \frac{2(2+v_i)(1-v_i)}{E_i} + \frac{2(2+v_j)(1-v_j)}{E_j} \tag{3b}$$

$$\frac{1}{R^*} = \frac{1}{r_i} + \frac{1}{r_j} \tag{3c}$$

where E_i and E_j are the elastic moduli of two contacting particles *i* and *j*; v_i and v_j are the Poisson's ratios of the particles *i* and *j*; r_i and r_j are the radii of the particles *i* and *j*. It is worth noting that the elastic modulus and Poisson's ratio are material constants,

while the particle radius and inter-particle overlap (δ_n) are variables being incrementally updated through the interactive process of DEM simulation. In this study, it is assumed that the elastic modulus and Poisson's ratio of each particle are identical (i.e., E_i=E_j, ν_i=ν_j). The values of the material parameters, e.g., elastic modulus and Poisson ratio are given in detail in section 4.2 Model geometry and parameters.

2.2 **Governing equations for computational fluid dynamics**

The CFD method solves the following continuity equation and locally averaged Navier-Stokes equation accounting for the presence of particles in the fluid.

$$\begin{cases} \dfrac{\partial(n\rho_f)}{\partial t} + \nabla\cdot(n\rho_f \mathbf{U}^f) = 0 \\ \dfrac{\partial(n\rho_f)}{\partial t} + \nabla\cdot(n\rho_f \mathbf{U}^f \mathbf{U}^f) - n\nabla\cdot(\mu\nabla\mathbf{U}^f) = -\nabla p - \mathbf{f}^p \end{cases} \tag{4}$$

where $\mathbf{U}^f$ and p is the average velocity and pressure of a fluid cell, respectively. n is the local porosity which is used to account for the particle influence on the fluid computation. ρ_f is the fluid density. The particle-fluid interaction force ($\mathbf{F}_i^f$) in Eq (1) is the fluid force acting on a single particle. The average particle-fluid interaction force ($\mathbf{f}^p$) in Eq (4) is the reaction force of the $\mathbf{F}_i^f$ within the volume of a fluid cell. The fluid force $\mathbf{f}^p$ is calculated as the summation of the fluid force acting on the particles in each fluid cell over the volume of the cell, i.e., $\mathbf{f}^p = \sum_{i=1}^{k} \mathbf{F}_i^f \big/ \Delta V$, where ΔV and k denote the volume of a CFD cell and number of particles in the cell, respectively. ρ and μ are the fluid density and viscosity, respectively. Numerically, the discretized cells are used to represent the continuous fluid domain. In each cell, variables such as density, fluid velocity and pressure are locally averaged quantities.

2.3 **Governing equations for particle-fluid interaction forces**

Previous research has shown that typical particle-fluid interaction forces include the drag force, pressure gradient force, buoyance force and viscous force, as well as other unsteady forces such as virtual mass force, Basset force and lift forces (Zhu et al., 2007). In a suffusion problem, the drag force, pressure gradient force and viscous force are usually considered significant (Hu et al., 2018; Hosn et al., 2018). Eq. 5 shows the particle-fluid interaction forces ($\mathbf{F}^f$) considered in this study including drag force ($\mathbf{F}^d$), pressure gradient force ($\mathbf{F}^p$) and viscous force ($\mathbf{F}^v$) as shown below:

$$\mathbf{F}^f = \mathbf{F}^d + \mathbf{F}^p + \mathbf{F}^v \tag{5}$$

The drag force is adopted from the expression proposed by Di Felice (1994), which is applicable for a dense granular regime and valid for a wide range of Reynolds numbers:

$$\begin{cases} \mathbf{F}^d = \dfrac{1}{8} C_d \rho_f \pi d_p^2 (\mathbf{U}^f - \mathbf{U}^p) \left| \mathbf{U}^f - \mathbf{U}^p \right| n^{1-\chi} \\ C_{\mathrm{d}} = \left(0.63 + \dfrac{4.8}{\sqrt{\mathrm{Re}_p}} \right)^2 \\ \mathrm{Re}_p = \dfrac{n \rho_f d_p \left| \mathbf{U}^f - \mathbf{U}^p \right|}{\mu} \\ \chi = 3.7 - 0.65 \exp[-\dfrac{(1.5 - \log_{10} \mathrm{Re}_p)^2}{2}] \end{cases} \tag{6}$$

where d_{p} is the diameter of particles and C_d is the particle-fluid drag coefficient for a single spherical particle that depends on the Reynolds number of the particle (Re_p). χ in Eq. 6 is a correlation function that modifies the coefficient of drag force accounting for the presence of other particles in the system.

The pressure gradient force ($\mathbf{F}^p$) and viscous force ($\mathbf{F}^v$) for a single particle are formulated by Eq. 7 and Eq. 8, respectively (Zhou et al., 2010):

$$\mathbf{F}^p = -V_p \nabla p \tag{7}$$

$$\mathbf{F}^v = V_p \nabla \cdot \boldsymbol{\tau} \tag{8}$$

where V_p is the volume of the particle. $\boldsymbol{\tau}$ is the viscous stress tensor which describes the friction between the fluid and the surface of particles.

3. Validation of coupled CFD-DEM method

This section aims to verify the coupled CFD-DEM method in the context of fluid-particle interaction (based on the locally-averaged Navier-Stokes equation (Anderson and Jackson, 1967)), which governs suffusion. The predictive capability of the method for simulating fluid-solid interaction for single and multi-particle is validated against two classic benchmarking examples, i.e., single spherical particle settling from air to water and upward seepage flow in a single column of spheres.

3.1 Single spherical particle settling from air to water

Sedimentation, or settling of particle into water, involves different particle-fluid interaction forces (i.e., drag force, pressure gradient force and viscous force), which are suitable for validating the coupled CFD-DEM method. Concha (2007) has given the analytical solution of the settling velocity of a sphere setting from air to water as follows:

$$u_p(t) = \frac{1}{18}\frac{(\rho_p - \rho_f) d_p^3 g}{\mu_f}[1 - \exp(-\frac{1}{27}\frac{\mu_f}{\rho_p d_p^3} t)] \tag{9}$$

where ρ_p and ρ_f are the density of the particle and fluid, respectively.

In the benchmarking simulation, a spherical particle of d_p=1 mm was dropped from a height of 45 mm from the centre of a container (see inset of Fig. 2(a)). The detailed information of the CFD-DEM model for this problem, including model geometry and parameters, is obtained from Zhao and Shan (2013). Fig. 2(a) compares the predicted and analytical results for the benchmarking example. It is evident that the predicted velocity of the particles in the water by the coupled CFD-DEM method is very similar to that calculated by the analytical solution, with a maximum percentage difference of smaller than 4.5%. This demonstrates the predictive capability of the CFD-DEM method for capturing the particle-fluid interaction force for a single particle.

3.2 **Upward seepage flow in a single column of spheres**

The phenomena of suffusion can be presented by simulating the seepage flow on sphere packings. The problem of upward seepage flow in a single column of spheres is a highly idealistic model for evaluating the fluid forces acting on massive particles during suffusion. The analytical solution for the settlement of the highest spheres without seepage flow was developed by Suzuki et al. (2007), as given below:

$$\delta = \frac{N(N+1)}{2k_n}\frac{4\pi}{3}\left(\frac{d}{2}\right)^3(\rho_p - \rho_f)g \tag{10}$$

where N and k_n are the number of particles and spring constant, respectively. d is the diameter of each particle. After the injection of upward seepage flow with a velocity of 0.005 m/s, the analytical solution for the displacement of the highest spheres in the column is given below (Suzuki et al., 2007):

$$S_t = \frac{u^*}{C_v}\frac{H^2}{2}\left(1-\frac{32}{\pi^3}\sum_{i=0}^{\infty}\frac{(-1)^i}{(2i+1)^3}e^{-T_v(2i+1)^2\pi^2/4}\right)$$
$$C_v = \frac{k}{m_v\rho_f g} \tag{11}$$
$$T_v = \frac{C_v t}{H^2}$$

where u^* is input flow velocity; T_v is time factor; C_v is the coefficient of consolidation; k is the coefficient of permeability; m_v is the coefficient of volume compressibility and H is the height of the column. The m_v can be directly evaluated from the highly idealized model while k is deduced from the experimental results by Ergun (1952) as follows:

$$k = \frac{u^*}{i} = \frac{\rho_f g}{\frac{1-n}{dn^3}\{150\frac{(1-n)\mu}{d}+1.75\rho_f u^*\}} \tag{12}$$

where n is porosity. Fig. 2(b) shows the initial tentative configuration of the CFD-DEM model for this problem. The model geometry and parameters involved in the CFD-DEM simulation are obtained from Suzuki et al. (2007).

Fig. 2(c) compares the predicted (by CFD-DEM method) and calculated (by Suzuki's analytical solution) settlement of the top particle without seepage flow. In this phase, the column of particles was only subjected to gravity and buoyancy. The calculated value was verified to be consistent with the theoretical value of 0.4278×10^{-3} m derived from Eq. 10. Fig. 2(d) compares the simulated and analytical displacement of the highest particle after the injection of upward seepage flow at a velocity of 0.005m/s. The simulated results are about 10% larger than the analytical solution. The reasonable agreement with the predicted and calculated results implicates that the coupled CFD-DEM method has an excellent performance in capturing interactions

between fluid and multi-particles.

4. Simulation program and model setup

4.1 Simulation program

The simulation in this study carried out 16 cases with typical range of F_c, p' and i to investigate their coupling effects on suffusion. Each gap-graded sample consists of particles with two diameters, i.e., coarse particles (D_c=1.0 mm) and fine particles (d_f=0.25 mm). The gap ratio D_c/d_f=4 was unstable according to the Kézdi method (Kézdi, 1979) and the Kenney and Lau criterion (Kenny and Lau, 1985). The low gap ratio and uniform diameter of the coarse and fine particles were adopted to reduce the total number of DEM particles for reasonable calculation efficiency. In the present study, the gap-graded soils are made of mono-dispersed fine and coarse particles, which is indeed unusual in DEM simulations. Mono-disperse materials are known to be prone to crystallization, particularly for samples with relatively low or high F_c. The reason of adopting such simple form of gap-graded soil (i.e., mono-dispersed) without considering crystallization is to reduce the computation time of each CFD-DEM simulation, which took at least 5~7 days even for sample with mono-dispersed grading. The shear stress (q) and soil density are not considered in this study. Both of them also have significant effects on suffusion (Chang and Zhang, 2013; Luo et al., 2019; Wauiter, 2019; Israr and Indraratna. 2019), which could be analyzed in future work.

Four different combinations between the fine and coarse particles were considered,

leading to four values of fine contents, i.e., F_c=20%, 25%, 30% and 35%. Fig. 3 shows the particle size distribution of the four types of gap-graded samples used in the simulation. It is worth noting that for the material considered in this study, the fine content transition from under-fill to over-filled microstructure is around 27%, which was quantified through a series of parametric study considering different fine contents (F_c=20, 25, 27, 30, 35%) and confining stresses (p'=50, 100 and 200 kPa). The resulted void ratios of the gap-graded samples with the given combinations of F_c and p' are shown in Fig. 4. It can be seen that the fine content threshold (corresponding to the minimum void ratio, or the maximum packing efficiency) for the material considered is 27%, irrespective of the p' value. Similar quantitative conclusion (i.e., fine content threshold is approximately 25%) was also made by the previous DEM studies (Shire et al., 2014). It was further revealed by these studies that for samples with F_c<25%, the fine particles under-fill the voids between coarse particles and play a diminished role in stress transfer. In contrast, when F_c>25%, the fine particles start to overfill the voids between coarse particles, exerting a significant effect on the entire force network of the sample.

A relatively lower and higher hydraulic gradient, i=0.2 and 2, ($i=\Delta p/\rho g L$, where Δp is the differential pressure and L is the sample length along the flow direction) were considered in this study to incorporate the effect of i on the evolution of suffusion. Three different levels of confining pressure were imposed on each sample under i=2. When i=0.2, high and low levels of confining pressure were imposed on the samples with

F_c=20% and 35%. Table 1 summarizes the details of the simulation program.

4.2 **Model geometry and parameters**

Fig. 5 shows a cubical permeameter test with stress-controlled boundaries simulated using the coupled CFD-DEM method. The length of the cubical sand sample was about 13.5 mm under p'=50, 100, 200 kPa. The CFD domain overlaps the DEM domain with the size of 14.5 mm×14.5 mm×19.0 mm, ensuring it entirely covering the DEM domain. The size of each fluid mesh is 2.9 mm×2.9 mm×3.2 mm, which is approximately 1.5~6.4 times of the particle diameter (i.e., 2.0 mm and 0.5 mm for the coarse and fine particles, respectively). As the fluid mesh is much larger than the grain size, the coupled CFD-DEM approach used in this study is spatially unresolved. The contact model between particles is the Hertz contact law, of which the adopted parameters in this study are approved to be appropriate for simulating sand (Widuliński et al., 2009). The fluid parameters are widely used water parameters in previous study (Zhao and Shan, 2013). Table 2 summarizes the properties of particles and fluid and numerical settings in the simulations.

To achieve numerical stability for CFD and DEM domain, the Courant number, defined in Eq. 13, should be below 0.2 and the time-step for DEM domain should be determined by the method proposed by Cundall and Strack (1979) as seen in Eq. 14.

$$C = \frac{\mathbf{U}^f \Delta t_f}{\Delta l} \tag{13}$$

where Δt_f is the fluid timestep and Δl is the minimum fluid cell length.

$$\Delta t \le 2\sqrt{\frac{M}{k}} \tag{14}$$

where M and k are the lowest particle mass of the compact and contact stiffness, respectively. Δt is the time-step for DEM domain. In this study, the fluid time-step was adopted as 1.0×10^{-4} s, ensuring that Courant number of all the simulations was an order of 10^{-3} which was low enough to ensure numerical stability for CFD. For the typical mass, size and stiffness considered in this study, the time step calculated from Eq. 14 is approximately 5×10^{-7} second. For the parameters in Table 2, it can be readily calculated that the maximum particle Reynolds number (Re_p) under a typical hydraulic gradient of i=2 is 5.6. This means the flows simulated in all the analyses reported herein fell within the laminar range (Re_p<10).

4.3 **Boundary conditions**

In the permeameter experiment, the hydraulic gradient along the soil sample was controlled by the fluid pressure at the inlet and outlet of the apparatus. The fluid pressures within the upstream and the downstream CFD domains with no grains are constant. The pressure gradient (i) seen by each sample is given by the imposed pressure drop divided by the granular sample length, which was remained either 0.2 or 2 during suffusion. Since gravity forces were not considered, i was simply a dimensionless rescaling of Δp (Wautier et al., 2019). The free slip boundary condition was applied on each lateral boundary, meaning that the surface fluid was restricted to move along the lateral boundaries.

For the boundary conditions of the DEM, isotropic stress (p' = 50 kPa, 100 kPa and 200 kPa) was applied to each boundary of each particle specimen using a servo wall algorithm. The confining wall was assumed to be rigid and perfectly smooth (i.e., μ_{wall}=0), with its normal stiffness being 10 times larger than that of particles. The bottom of each specimen was supported vertically by a downstream wall, which was fixed in both vertical and horizontal directions. To allow the escape of the eroded particles from the samples, a series of holes with size 0.875mm ×0.875mm (1.75 times the fine particle diameter) was set at an equal-spacing (0.125 mm) on the downstream wall.

4.4 **Simulation procedure**

Each cubic assembly of spheres was first generated randomly with the prescribed gradation as shown in Fig. 3 and isotopically loaded by six surrounding walls to the target level of confining pressure. The inter-particle friction coefficient was maintained at a relatively low value of 0.1 during the sample preparation processes (i.e., generating particles and applying confining stress to the sample), with the intention to produce medium dense samples. The resulted relative densities of the samples are in the range between 58.8% and 70.2%. The relative density of each sample is calculated by the following equation:

$$R_d=(e_{max}-e)/(e_{max}-e_{min}) \quad (15)$$

where e is the void ratio of the sample; e_{max} and e_{min} are the maximum and minimum void ratios of the sample, respectively. Following Salot et al. (2009)'s method, the maximum and minimum void ratios are achieved by setting the coefficients of inter-

particle friction μ=0.0 and 1.0 during the isotropic compression stage of the least and the most dense samples, respectively.

After the sample preparation and before applying seepage flow, the inter-particle friction coefficient is increased to 0.3. The unbalanced force within the DEM samples, which was defined in Eq. 16, was found to stay below 0.01 (Wautier et al., 2019) before the initiation of the suffusion simulation.

$$F_{\text{unb}} = \frac{\frac{1}{N_p}\sum_{p=1}^{N_p}\left\|F_p\right\|}{\frac{1}{N_c}\sum_{c=1}^{N_c}\left\|F_c\right\|} \tag{16}$$

where F_{p} is the sum of all contact forces acting on particle p and F_{c} is the contact force between two particles. N_{p} and N_{c} are the number of particles and contacts, respectively. After generation of the initial DEM sample, a differential hydraulic pressure was imposed on the upstream and downstream of each gap-graded sample to model suffusion. Table 3 summarizes the number of simulated particles and micromechanical properties of each sample, including fines content, void ratio and relative density.

During each simulation, the pressure applied to the six surrounding walls of each sample remained constant. The particles that flowed out of the downstream wall were deemed as eroded particles. The information for all particles (including position, velocity and drag force etc.) and all contact forces and energies within the samples were all recorded into files at every 0.05 s during each suffusion simulation with a total duration of 14.0 seconds. Each simulation that model 14 seconds of physical time of suffusion in this study took approximately 5~7 days on a HP station with 8 Intel Xeon

E52680-v4 2.4GHz processors and 512GB DDR4 RAM. Although the simulation duration is relatively short (i.e., 14 s) as compared to that in a laboratory test, this duration has largely covered the key stages for suffusion involved in each analysis, i.e., initiation, intensified suffusion following initiation, and a gradually stabilized response. In other words, each simulation reported herein has contained key macro- and microscopic mechanisms on the suffusion of gap-graded soil. On the other hand, the short physical time is sufficient to describe suffusion in DEM because of the numerical sample dimension is very small (i.e., the length is about 13.5 mm) compared with that of the experimental sample (i.e., the length is about 100-150 mm). A sample of the "numerical dimensions" inside a real lab sample would see some perturbations coming from the rest of the sample during the suffusion test (e.g., input of new particles in the upstream, modification of the stress state etc.). As a result, the final state is longer to reach in the experiments.

5. Simulation Results

5.1 Macro responses of the gap-graded samples to suffusion

Fig. 6(a) shows the percentage of cumulative fines loss with time for the samples having different initial fines contents (F_c=20% and 35%) and confining pressures subjected to a given hydraulic gradient of 0.2. Only results for the sample with F_c=20% and 35% were illustrated because the critical fines content at which the fines fill the voids is about 27% for the sample considered in this study. It is noted that the cumulative fines loss was decreased with confining pressure for all samples, meaning

that high confining pressure helped to resist the erosion of fines caused by seepage flow with a relatively low hydraulic gradient. Many previous studies (Richards and Reddy, 2010; Li and Fannin, 2012; Luo et al., 2013; Chang and Zhang, 2013; Liang et al., 2017) has also confirmed this observation, attributing it to stronger contact forces between particles imposed by high confinements (Shire et al., 2014). The load-bearing skeleton of the sample was relatively stable under the condition of a low hydraulic gradient, so that only fines with small contact forces were eroded. Figs. 6(b) and (c) show that no excessive deformation for each sample was observed under the condition of i=0.2, meaning that the load-bearing skeleton of each sample was stable during suffusion.

However, if i was increased to a sufficiently large value to destabilize the original load-bearing skeleton (usually occurs in backward erosion), the confining pressure was found to intensify suffusion. Fig. 7(a) shows the percentage of cumulative eroded particles for the samples with F_c=20% (i.e., fines underfilled the voids between coarse grains) and 35% (i.e., fines overfilled the voids between coarse grains) under p'=50, 100 and 200 kPa when i=2.0. In contrast with the results when i=0.2, the cumulative eroded soil mass for all samples increased with the effective confining pressure, meaning that the confining pressure facilitated the transportation and erosion of the fine particles, especially for the sample with F_c=35% (i.e., fines overfilled the voids between coarse grains). This is probably because the fines overfilled the voids between coarse particles and participated heavily in load-bearing for the sample with F_c=35%. The erosion of fines under high i could cause the collapse of the original force transmission

structure. The release of higher strain energy within samples under higher p' accelerated particle movement and intensified suffusion. Detailed micro-mechanical analyses are given in subsections 5.2-5.4. This tendency is in accordance with the experimental findings made by Tomlinson and Vaid (2000), Papamichos (2001), Bendahmane et al. (2008) and Chang (2013).

The curves for the sample with F_c=35% (i.e., fines overfilled the voids between coarse grains) under i=2.0 indicate that after the initiation of suffusion, the eroded particles mass and deformation of the sample both increase dramatically. Figs. 8(a) to (d) show that the axial and radial deformation of each sample under i=2.0, which are consistent with the corresponding cumulative eroded particles mass. The moment for the sudden increase of eroded fines loss and the sample deformation in the case of F_c=30% and 35% (see Figs. 7 and 8) is called turning point in this study. The basic physical cause of the turning point is the strong force chain buckling and the associated collapse of the force transmission structure of the sample, with a substantial increase in the eroded fines loss and the appearance of significant kinetic energy of total particles. A detailed analysis of the physical cause of the turning point is given in sections 5.3 and 5.4. The subsequent analyses will focus on the effects of confining pressure on the suffusion behavior of the samples containing different fines contents under i=2.0.

To check if a regressive erosion occurs in the simulations of this study, Fig. 9 shows the vertical profile of fines content before and after erosion for the samples with F_c=20% and 35% under p'=50 kPa. It can be observed that the fine particles in the top

four layers are migrated from the upstream to the downstream region during suffusion, suggesting that the regressive erosion is not likely to occur within the whole sample. The particles at the bottom layer are significantly eroded due to the circular holes in the downstream confining wall.

Two distinct macro responses to confining pressure for the sample with F_c=20% (i.e., fines underfilled the voids between coarse grains) and 35% (i.e., fines overfilled the voids between coarse grains) stems from the structure of the soil packings as shown in the inset of Fig. 7. For the samples with F_c=35% (i.e., fines overfilled the voids between coarse grains), the fines overfill the voids between coarse particles, separating the coarse particles and forming a load-bearing skeleton. In this case, the erosion of fines has significant effects on the entire force network of the sample. While for the samples with F_c=20% (i.e., fines underfilled the voids between coarse grains), the fines underfill the voids between coarse particles with little contribution to the load-bearing skeleton. Even though the fine particles were gradually eroded under i=2.0, the original load-bearing skeleton remains stable which was similar with the condition of i=0.2. Fig. 7(b) shows that the suffusion behavior for the samples with F_c=25% (i.e., fines underfilled the voids between coarse grains) and 30% (i.e., fines overfilled the voids between coarse grains) has a similar tendency stated above.

In order to further understand the characteristics of the two typical structures of soil packing, Figs. 10 and 11 show the initial sample profile, contact force and strain energy for the samples with F_c=20% (i.e., fines underfilled the voids between coarse

grains) and F_c=35% (i.e., fines overfilled the voids between coarse grains) under p'=50 and 200 kPa. The strain energy of each contact consists of a normal (E_{sn}) and a shear component (E_{st}), which are calculated by Eqs. 16 and 17, respectively (Hanley et al., 2018):

$$E_{sn} = \frac{2}{5}\left|F_n\right|s \tag{17}$$

$$E_{st} = E_{st}^{\beta-1} + \frac{\left|F_t^{\beta-1} + F_t^{\beta}\right|}{2}\frac{\left|F_t^{\beta} - F_t^{\beta-1}\right|}{k_t} \tag{18}$$

where F_n and s are the normal force and inter-particle overlap of the contact, respectively. $E_{st}^{\beta-1}$ is the tangential component of strain energy at previous time-step β-1. F_t^{β} and $F_t^{\beta-1}$ are the tangential force of the contact at current and previous time-step, respectively. k_t is the contact shear tangential stiffness. It is observed from Figs. 11 and 12 that for the samples with F_c=35% (Fig. 12), the contacts with larger forces contain more strain energy. The fines overfill the voids between coarse particles, separating the coarse particles and forming a load-bearing skeleton. In this case, the erosion of fines has significant effects on the entire force network of the sample. If the load-bearing skeleton of the samples collapses, more fines will be eroded (Bendahmane et al, 2008; Liang et al., 2017) owing to the weakened contact forces acting on fines and the release of strain energy stored in these contacts. The collapse of stronger contact forces within samples under higher p' causes more strain energy to release which will intensify suffusion (detailed analysis in Section 5.4).

While for the samples with F_c=20% (i.e., fines underfilled the voids between coarse grains), the profile of contact forces (Fig. 11) shows the magnitude of coarse-

fine contact forces is small which implies that fines underfill the voids between coarse particles with little contribution to the load-bearing skeleton (Chang and Meidani, 2013; Ke and Takahashi, 2015). The external force of the soil skeleton is mainly transmitted by coarse particles (Minh et al., 2014), which means that p' hardly influences the number and magnitude of contact forces acting on fines. Thus, the loss of fines due to suffusion is slightly affected by p'. Novel ground improvement techniques such as Microbially Induced Calcite Precipitation (MICP) may help to prevent suffusion of gap-graded soils (Wu and Chu, 2019; Wu et al., 2019).

5.2 **The role change of different networks during suffusion**

The contribution of various contact networks to the overall external confining pressure, which is calculated by Eq. 19, can be used to reflect the mechanical consequences of suffusion for different fractions within a sample.

$$\begin{aligned} c_{net} &= p'_{net} / p' \\ p'_{net} &= \frac{1}{3}\sigma_{ii} \\ \sigma_{ij} &= \frac{1}{V}\sum_{c\in net} f_i^c d_j^c \end{aligned} \tag{19}$$

where *net* denotes the different strong or weak networks formed by the overall contacts, coarse-coarse/fine contacts or fine-fine contacts. Coarse-coarse/fine contacts denote the meeting of the coarse-coarse and coarse-fine contacts. p'_{net} is the confining pressure constituted by a network. c_{net} means the contribution of a network to the overall confining pressure. V is the total volume of the assembly. In this study, the average normal forces ($\overline{f}_n$) are used to distinguish the strong and weak network (Radjai et al.,

1998; Thornton and Antony, 1998). f_i^c is the contact force at a contact and d_j^c is the branch vector joining the centers of two contacting particles.

Figs. 12(a) and 12(b) show that the contribution and the fraction of various contact networks to confining pressure in the process of suffusion respectively for the samples with F_c=35% (i.e., fines overfilled the voids between coarse grains) under p'=50kPa and i=2.0. For this kind of sample, the contribution of the weak network constituted by the fine-fine contacts decreased before turning point while the contribution of the strong network constituted by the coarse-coarse/fine contacts increased, leading to a change in contribution of the overall strong and weak network to confining pressure. This is because in this phase the fines with low connectivity and contact forces were eroded first (Kawano et al., 2018; Hu et al., 2019), resulting in stronger contact forces within the overall strong network.

After the turning point, Figs. 12(a) and 12(b) show that both the contribution and the fraction of the overall strong network experienced a sudden change. The contribution of the strong network increased significantly (Fig. 12(a)), whereas the fraction of the strong network decreased (Fig. 12(b)). The weak network of the whole sample displayed the opposite trend. Another important fact is that after the turning point coarse particles played a more important role in the load-bearing skeleton as shown in Fig. 12(a), and the fine-fine contact forces were weakened. This is validated by Fig. 12(b), which shows that the fraction of strong network constituted by fine-fine contacts decreased. These trends are consistent with the study by Minh et al. (2014),

revealing that the contribution of fine-fine strong contacts reduced rapidly with the decrease of fines content while the contribution of the coarse-coarse/fine contacts increased.

For the sample with F_c=20% (i.e., fines underfilled the voids between coarse grains) under p'=50 kPa and i=2.0, Fig. 13(a) illustrates how the contribution of different networks to the confining pressure remained constant during suffusion, meaning that the erosion of fines had little influences on the load-bearing skeleton. Fig. 13(b) shows that the fraction of different networks for the sample also changed slightly during suffusion.

5.3 **Strong force chain buckling**

In comparison with the sample with F_c=20%, (i.e., fines underfilled the voids between coarse grains) the contribution and the fraction of the strong and weak networks for the sample with F_c=35% (i.e., fines overfilled the voids between coarse grains) experienced a sudden change during suffusion (Fig. 7), after which the original load-bearing skeleton collapsed and a new skeleton was eventually formed. The collapse of the original load-bearing skeleton was mainly induced by the strong force chain buckling. Figs. 14 and 15 show the evolution of the local specimen profile and the contact force chains during suffusion at the same position of the samples with F_c=20% and F_c=35%, respectively. The strong force chains and the chained particles are marked in red. The strong force chain was defined in this study as three particles connecting in a quasi-linear mode, as shown in Fig. 14, where the contact forces between particles

were larger than the average value. According to Tordesillas (2009) and Tordesillas et al. (2014), force chain buckling occurs if the intersection angle of the chains is reduced by 1° in a short time (i.e., δt=0.001s). In this study, the above geometry variation criterion together with 50% reduction of the force chain magnitude was adopted to define strong force chain buckling. The particles in contact with the chained particles were also plotted to show the consequences of strong force chain buckling to the neighboring particles. Fig. 14 shows that for the sample with F_c=35% (i.e., fines overfilled the voids between coarse grains), the magnitude of strong force chain increased obviously from the initial time to the turning point, implying that the external force was transferred from the weak contact forces to the strong contact forces due to the fines loss. This is consistent with the observed increase in the confining pressure of the strong network, as shown in Fig. 12(a). At the turning point, for the sample with F_c=35% (i.e., fines overfilled the voids between coarse grains), the coarse particle deviated from its original position in a short time, accompanying an apparent decrease of the angle between the strong force chains. At the same time, the magnitude of the force chain became minor. Such angel deflection and decrease of force chain magnitude are main characters of force chain buckling (Tordesillas, 2009; Nicot et al., 2017).

Fig. 15 shows the evolution of local specimen profile during suffusion for samples with F_c=20% (i.e., fines underfilled the voids between coarse grains). It should be noted that the local specimen profile as shown in Fig. 14 and 15 were located in the same area of the respective samples. In this case, the bearing load skeleton was primarily

constituted by coarse-coarse contacts (Figs. 10(a) and 10(b)). The fines only underfilled the voids between coarse particles and their erosion had little influences on the strong coarse-coarse contacts. Fig. 15 shows that the strong force chain marked in red was stable throughout the suffusion process. This was in accordance with the previous analysis that the role of the strong network slightly changed during suffusion in this case.

Fig. 16 shows the axial force of the strong force chains in Figs. 14 and 15 in the case of p'=50 kPa, 200 kPa and i=2.0. For samples with F_c=35% (i.e., fines overfilled the voids between coarse grains), the axial force gradually increased before the turning point, implying that the external force was transferred to the strong force chain. At the turning point, the axial force reached its maximum value and then decreased to a minor value. For samples with F_c=20% (i.e., fines underfilled the voids between coarse grains), Fig. 16(a) shows that the axial force of the strong force chain was unchanged during the suffusion process. The decrease of the contact force between particles thus made the particles more vulnerable to detach (Zhang et al., 2018; Kawano et al., 2018; Hosn et al., 2018). Fig. 16(b) shows the angle magnitude of the strong force chain in Figs. 14 and 15. The angle magnitude (θ) is illustrated in the inset of Fig. 16(b). It is defined as the angle (in degree) between two vectors which pointing from the center of a particle (particle 2, see inset of Fig. 16(b)) to that of its two neighboring particles (particles 1 and 3, see inset of Fig. 16(b)) in a force chain. The apparent decrease of the strong force chain angle for samples with F_c=35% (i.e., fines overfilled the voids between coarse

grains) indicated that the force chain buckled at the turning point in these cases. For samples with F_c=20% (i.e., fines underfilled the voids between coarse grains), the force chain angle was constant during suffusion, which was in accordance with behavior of the local specimen profile as shown in Fig. 15.

Fig. 17 shows the evolution of the ratio of the average contact force to the fluid force (F_{cont}/F_{fluid}) for the fine particles in a local packing of the sample with F_c=35% under p'=50 kPa. The average contact forces for the fine particles in the local packing are 2~6 times the fluid forces applied to them at the initiation of suffusion. It is observed that several fine particles with a low F_{cont}/F_{fluid} are first detached from the chained particles at about 2.1 s. The ratios of the average contact forces to the fluid forces for these fine particles continue to decrease before being eroded. These fine particles around chained particles involve in the force chain and provide more important lateral support. When a certain amount of the fine particles providing the lateral support are lost, the buckling of the chained particles occurs, as shown in the inset of Fig. 17 and Fig. 14. Subsequently, more fine particles supported by the chained particles are released and eroded at 3.6 s, as shown in the inset of Fig. 17. The F_{cont}/F_{fluid} for some remaining fine particles increases obviously due to the stress transfer during the rearrangement of the particles.

Previous analyses show that strong force chain buckling weakened the contact forces on fine particles (Bi et al., 2011; Nguyen, 2016; Nicot et al., 2017) and then facilitate the erosion of these fine particles. To explain the different effects of p' on the

cumulative fines loss as shown in Figs. 7 and 8, Fig. 18 shows the percentage by quantity of buckled strong force chains during suffusion for the samples with F_c=20% and 35% under p'=50 and 200 kPa. Fig. 18 shows that the percentage by quantity of the buckled strong force chains increased dramatically at the turning point for samples with F_c=35% (i.e., fines overfilled the voids between coarse grains) under p'=50 and 200 kPa. After the sudden increase of the buckling fraction, the eroded particles mass also increased as shown in Fig. 7. Further inspection into the computed results reveals that the erosion intensification following force chain buckling is linked to the release of new free particles. For the sample with higher confining pressure (p'=200 kPa), the buckling fraction was larger, resulting in a larger eroded particles mass under this condition. As the discharge of eroded fine particles stabilized, the buckling fraction degraded gradually for the samples with F_c=35% under both confining pressures. Due to the short simulation time, the sample was hardly stable when subjected to seepage flow, resulting in the existence of an appreciable buckling fraction at the final stage. While for the samples with F_c=20% (i.e., fines underfilled the voids between coarse grains), under both confining pressures, the fraction of buckled strong force chains remained small and constant during suffusion, meaning that the original load-bearing skeleton was stable.

5.4 **Energy evolution during suffusion**

The strong force chain buckling and induced collapse of the strong network caused

the strain energy stored in the contacts to be released, especially the strain energy within strong fine-fine contacts.

Fig. 19 shows the evolution of the strain energy within strong fine-fine contacts during suffusion for samples with F_c=20% and 35% under p'=50 and 200 kPa. At the turning point, the strain energy within strong fine-fine contacts started to decrease for samples with F_c=35% (i.e., fines overfilled the voids between coarse grains) under both confining pressures. It was noted that the strain energy in the sample with higher confining pressure (p'=200 kPa) experienced the greatest decrease due to strongest contact forces acting on the fines. For samples with F_c=20% (i.e., fines underfilled the voids between coarse grains), the strain energy within strong fine-fine contacts was almost not released during suffusion. This was because the external force was primarily transmitted by coarse particles for this sample as show in Fig. 15. The strain energy within fine-fine contacts was relatively lower than that of the sample with F_c=35% (i.e., fines overfilled the voids between coarse grains) due to the small magnitude of fine-fine contact forces.

The release of strain energy due to the collapse of the strong network will accelerate particle movement. Fig. 20 shows the kinetic energy of fine and coarse particles in samples with different fines contents and confining pressures. The kinetic energy of a particle in this study is the summation of its translational and rotational kinetic energies which are respectively calculated as (Hanley et al., 2018)

$$E_{kt} = \frac{1}{2}\sum_{i=1}^{N_p} m_i v_i^2 \tag{20}$$

$$E_{kr} = \frac{1}{2}\sum_{i=1}^{N_p} I_i \omega_i^2 \tag{21}$$

where m_i is the mass of particle i. v_i and ω_i are the translational and rotational speed of particle i, respectively. N_p is the total number of fine particles. $I_i = 0.4 m_i r_i^2$ is the moment of inertia of particle i.

For the samples with F_c=35% (i.e., fines overfilled the voids between coarse grains), the kinetic energy of both kinds of particles increased dramatically after the turning point due to strong force chain buckling (Bi et al., 2011; Nguyen, 2016; Nicot et al., 2017), which intensified suffusion. In contrast, before the turning point, only particles in the weak network had high kinetic energy because in this phase the strong network of the sample was relatively stable and only fines with low connectivity and contact forces were eroded. Figs. 20(a) and 20(b) also shows that kinetic energy of the particles in the sample under higher confining pressure was higher than that under lower confining pressure, which is consistent with the extent of the released strain energy for the respective samples. Figs. 20(c) and 20(d) show that the kinetic energy of fines in the sample with F_c=20% (i.e., fines underfilled the voids between coarse grains) was much lower than that of the sample with F_c=35% (i.e., fines overfilled the voids between coarse grains) due to lower released strain energy of fines.

Fig. 21 shows the cumulative eroded mass of fines in the strong and weak networks for the samples with F_c=35% (i.e., fines overfilled the voids between coarse grains)

under p'=50 and 200 kPa. It is obvious that after the turning point the fines in the strong network (the fine particles with contact forces of which the magnitude is larger than the average contact forces) started to be eroded, which is consistent with the variation of the kinetic energy of strong network before and after the turning point. The mechanical instability of gap-graded soil subjected to suffusion, as discussed above, is interpreted in the context of evolving kinematic and strain energies. This instability problem should be further analyzed using the second order work criterion, which remains to be the authors' future pursuit.

6. Conclusions and discussion

This study presents a coupled CFD-DEM investigation, with the aim to understand the coupling effect of p' and F_c on the erodibility of gap-graded coarse-grained soil, and to shed micromechanical insights into the phenomenon. Typical ranges of F_c (20% to 35%) and p' (50 to 200 kPa) are considered. The simulated results of eroded particles mass and samples deformation were presented and interpreted from a micromechanical perspective, including the evolution of force transmission structure, force chain buckling and strain energy release under the action of suffusion.

It is revealed from the coupled CFD-DEM investigation that when the fines overfilled the voids between coarse particles (i.e., F_c >25%) and participated heavily in load-bearing, the erosion of the fines (triggered by a hydraulic gradient i=2 in this study) could lead to the buckling of the strong force chains, and cause a significant collapse

of the original force transmission structure. The sudden collapse has facilitated particle movement and strain energy release, which intensified suffusion. The aforementioned observations become more pronounced for a higher confining stress p'.

On the contrary, for the samples with the fines underfilled the voids between coarse particles (i.e., F_c<25%), only fines that do not fill the voids were eroded which had little influence on the force network. High confining pressure in this case increased the contact forces between fines, which may had served as a stabiliser to maintain the contact structure and prevent the occurrence of suffusion.

The notion of active fine fraction could be used to understand the consequences of suffusion for large F_c. The concept of preferential growth of contact forces (Pouragha et al., 2019) can help understand the poor influence of p' on the eroded mass observed in this study. Indeed, if contact forces increase as a fraction of their current value under an increase in p', the weak contact force does not increase much in absolute value (Pouragha et al., 2019) and remain small enough with respect to fluid forces. The definition of force chain as well as buckling of force chains is introduced but the influence of the topology of the surrounding weak phase could be investigated more deeply as it is known to control force chain stability (Tordesillas et al., 2011). For large F_c, fine particles are probably more involved in force chains (Shire et al., 2016) and in the same time the weak phase provides a more important lateral support (Wautier et al., 2018). Under such hypothesis, an erosion of some fine particles will lead to more dramatic consequences.

7. Acknowledgements

The authors gratefully acknowledge the financial supports from the National Key Research and Development Program (2016YFC0800200), the Key Research and Development Program of Zhejiang Province (2018C03031), National Natural Science Foundation of China (51939010 and 51779221) and GRF project (Grant No. 15209119) from Research Grants Council (RGC) of Hong Kong.

References

Anderson TB, Jackson R. Fluid mechanical description of fluidized beds. Equations of motion, Industrial and Engineering Chemistry Fundamentals 6 (1967) 527–539

Bendahmane F, Marot D, Alexis A. Experimental parametric study of suffusion and backward erosion. J. Geotech. Geoenvironmental. Eng. 2008, 134, 57-67.

Bi ZW, Sun QC, Jin F, Zhang M. Numerical study on energy transformation in granular matter under biaxial compression. Granular Matter. 2011, 13, 503-510.

Cundall PA, Strack ODL. A discrete numerical model for granular assemblies. Geotechnique. 1979, 29(1), 47-65.

Chang CS, Meidani M. Dominant grains network and behavior of sand-silt mixtures: stress-strain modeling. Int. J. Numer. Anal. Meth. Geomech. 2013, 37(15), 2563-2589.

Chang DS, Zhang LM. Critical Hydraulic Gradients of Internal Erosion under Complex Stress States. J. Geotech. Geoenvironmental. Eng. 2013, 139(9), 1454-1467.

Concha F. Settling velocities of particulate systems. KONA Powder and Particle Journal. 2009, 27, 18-37.

Chang DS. Internal erosion and overtopping erosion of earth dams and landslide dams. PhD thesis. 2012. Hong Kong University of Science and Technology.

Di Felice R. The voidage function for fluid-particle interaction systems. Intl J. Multiph. Flow. 1994, 20, 153-159.

Ergun S. Fluid flow through packed columns. Chem. Eng. Prog. 1952, 48(2), 89-94.

Goniva C, Kloss C, Deen NG et al. Influence of rolling friction on single spout fluidized bed simulation. Particuology. 2012, 10, 582-591.

Hanley KJ, Huang X, O'Sullivan. Energy dissipation in soil samples during drained triaxial shearing. Géotechnique. 2018, 68(5):421-433.

Hosn RA, Sibillea L, Benahmedb N, Chareyre B. A discrete numerical model involving partial fluid-solid coupling to describe suffusion effects in soils. Computers and Geotechnics. 2018, 95, 30-39.

Hu Z, Zhang YD, Yang ZX. Suffusion-induced deformation and microstructural change of granular soils: a coupled CFD-DEM study. Acta Geotechnica. 2019, 14(3), 795-814.

Israr J, Indraratna B. Internal stability of granular filters under static and cyclic loading. J. Geotech. Geoenviron. Eng., 2017, 143(6): 04017012.

Israr J, Indraratna B. Study of critical hydraulic gradients for seepage-induced failures in granular soils. J. Geotech. Geoenviron. Eng. 2019, 145(7): 04019025.

Jin, T., Luo, K., Fan, J. and Yang, J. Immersed boundary method for simulations of erosion on staggered tube bank by coal ash particles. Powder technology, 2012, 225, 196-205.

Kloss C, Goniva C, Hager A, Amberger S, Pirker S. Models, algorithms and validation for opensource DEM and CFDDEM. Progr. Comput. Fluid Dyn. 2012, 12(2-3), 140-152.

Kawano K, Shire T, O'Sullivan C. Coupled particle-fluid simulations of the initiation of suffusion. Soils and Foundations. 2018, 58(4), 972-985.

Ke L, Takahashi A. Drained monotonic responses of suffusional cohesionless soils. J. Geotech. Geoenvironmental. Eng. 2015, 141, 4015033.

Ke L, Takahashi A. Experimental investigations on suffusion characteristics and its mechanical consequences on saturated cohesionless soil. Soils and Foundations. 2014, 54(4), 713-730.

Kezdi, A. Soil physics-selected topics. Elsevier Scientific Publishing Co., Amsterdam, 1979.

Kenney TC, Lau D. Internal stability of granular filters. Can. Geotech. J. 1985, 22(2), 215-225.

Kloss C, Goniva C, Hager A et al. Models, algorithms and validation for opensource DEM and CFD-DEM. Prog. Comput. Fluid. Dyn. Int. J. 2012, 12, 140-152.

Li M, Fannin RJ. A theoretical envelope for internal instability of cohesionless soil. Géotechnique. 2012, 62(1), 77-80.

Luo YL, Jin X, Li X, Zhan ML, Sheng JC. A new apparatus for evaluation of contact erosion at the soil-structure interface. Geotechnical Testing Journal. 2013, 36, 256-263.

Luo YL, Luo B, Xiao M. Effect of deviator stress on the initiation of suffusion. Acta Geotechnica. 2019. https://doi.org/10.1007/s11440-019-00859-x.

Liang Y, Yeh TCJ, Wang JJ, Liu MW, Zha YY, Hao YH. Onset of suffusion in upward seepage under isotropic and anisotropic stress conditions. European Journal of Environmental and Civil Engineering. 2017.

Mindlin RD, Deresiewicz H. Elastic spheres in contact under varying oblique forces. Transactions of ASME, Series E. Journal of Applied Mechanics. 1953, 20, 327-344.

Minh NH, Cheng YP, Thornton C. Strong force networks in granular mixtures. Granular Matter. 2014, 16, 69-78.

Nguyen HNG, Prunier F, Djéran-Maigre I, Nicot F. Kinetic energy and collapse of granular materials. Granul. Matter. 2016, 18, 1-10.

Nicot F, Xiong H, Wautier A, Lerbet J, Darve F. Force chain collapse as grain column buckling in granular materials. Granular Matter. 2017, 19, 18(1-12).

Nguyen CD, Nadia Benahmed, Edward Ando, Luc Sibille, Pierre Philippe. Experimental investigation of microstructural changes in soils eroded by suffusion using X-ray tomography. Acta Geotechnica. 2019. https://doi.org/10.1007/s11440-019-00787-w.

Papamichos E, Vardoulakis I, Tronvoll J, Skjvrstein A. Volumetric sand production model and experiment. Int. J. Numer. Anal. Meth. Geomech. 2001, 25, 789-808.

Pouragha M, Duriez J, Wautier A, Wan R, Nicot F, Darve F. Preferential growth of force network in granular media. Granular Matter. 2019, 21, 67. https://doi.org/10.1007/s10035-019-0919-1.

Richards KS, and Reddy KR. True triaxial piping test apparatus for evaluation of piping

potential in earth structures. J. ASTM Geotech Test. 2010, 33(1), 83-95.

Renzo AD, Maio FPD. Comparison of contact-force models for the simulation of collisions in DEM-based granular flow codes. Chemical Engineering Science. 2004, 59(3), 525-541.

Radjai F, Wolf D, Jean M, Moreau JJ. Bimodal character of stress transmission in granular packings. Phys. Rev. Lett. 1998, 80, 61-64.

Salot C, Gotteland P, Villard, P. Influence of relative density on granular materials behavior: DEM simulations of triaxial tests. Granular Matter. 2009, 11, 221-236. https://doi.org/10.1007/s10035-009-0138-2.

Shire T, O'Sullivan C. Micromechanical assessment of an internal stability criterion. Acta Geotechnica. 2013, 8, 81-90.

Shire T, O'Sullivan C, Hanley KJ, Fannin RJ. Fabric and effective stress distribution in internally unstable soils. J. Geotech. Geoenvironmental. Eng. 2014, 140(12), 04014072.

Shire T, O'Sullivan C, Hanley KJ. The influence of fines content and size-ratio on the micro-scale properties of dense bimodal materials. Granular Matter. 2016, 18, 52. https://doi.org/10.1007/s10035-016-0654-9.

Suzuki K, Bardet JP, Oda M, Iwashita K, Tsuji Y, Tanaka T, Kawaguchi T. Simulation of upward seepage flow in a single column of spheres using discrete-element method with fluid-particle interaction. J. Geotech. Geoenvironmental. Eng. 2007, 133(1), 104-109.

Thornton C, Antony SJ. Quasi-static deformation of particulate media. Philos. Trans. R. Soc. A. 1998, 356, 2763-2782.

Tordesillas A, Zhang J, Behringer R. Buckling force chains in dense granular assemblies: Physical and numerical experiments. Geomechanics and Geoengineering: An International Journal. 2009, 4, 3-16.

Tordesillas A, Lin Q, Zhang J, Behringer RP, Shi J. Structural stability and jamming of self-organized cluster conformations in dense granular materials. Journal of the Mechanics and Physics of Solids. 2011, 59, 265-296.

Tordesillas A, Steer C, Walker D. Force chain and contact cycle evolution in a dense granular material under shallow penetration. Nonlinear Processes in Geophysics. 2014, 21, 505-519.

Tomlinson SS, Vaid YP. Seepage forces and confining pressure effects on piping erosion. Can. Geotech. J. 2000, 37, 1-13.

Wang, M., Feng, Y.T., Pande, G.N., Chan, A.H.C. and Zuo, W.X. Numerical modelling of fluid-induced soil erosion in granular filters using a coupled bonded particle lattice Boltzmann method. Computers and Geotechnics, 2017, 82, 134-143.

Wang, M., Feng, Y.T., Owen, D.R.J. and Qu, T.M. A novel algorithm of immersed moving boundary scheme for fluid–particle interactions in DEM–LBM. Computer Methods in Applied Mechanics and Engineering, 2019, 346, 109-125.

Wang S, Chen JS, Luo YL, Sheng JC. Experiments on internal erosion in sandy gravel foundations containing a suspended cutoff wall under complex stress states. Nat

Hazards. 2014, 74, 1163-1178.

Wautier A, Bonelli S, Nicot F. Flow impact on granular force chains and induced instability. 2018. Pysical review E. 98, 042909.

Wautier A, Bonelli S, Nicot F. DEM investigations of internal erosion: Grain transport in the light of micromechanics. Int. J. Numer. Anal. Meth. Geomech. 2019, 43, 339-352.

Widuliński L, Kozicki J, Tejchman J. Numerical simulations of triaxial test with sand using DEM. Archives of hydro-engineering and environmental mechanics. 2009, 56(3-4), 149-171.

Wu C, Chu J. Biogrouting method for stronger bond strength for aggregates. Journal of Geotechnical and Geoenvironmental Engineering (ASCE). 2019, 10.1061/(ASCE)GT.1943-5606.0002386.

Wu C, Chu J, Wu S, Cheng L, von Paassen L. Microbially Induced Calcite Precipitation along a Circular Flow Channel under a Constant Flow Condition. Acta Geotechnica. 2019, 14(3), 673-683. https://doi.org/10.1007/s11440-018-0747-1

Xiong H, Yin Z-Y, Zhao J, Yang Y. Investigating the effect of flow direction on suffusion and its impacts on gap-graded granular soils. Acta Geotech. 2020. DOI: 10.1007/s11440-020-01012-9.

Yang J, Yin Z-Y, Laouafa F, Hicher P-Y. Internal erosion in dike-on-foundation modeled by a coupled hydro-mechanical approach. Int. J. Numer. Anal. Methods Geomech. 2019, 43(3):663-683.

Yang J, Yin Z-Y, Laouafa F, Hicher P-Y. Three-dimensional hydro-mechanical modelling of internal erosion in dike-on-foundation. Int. J. Numer. Anal. Methods Geomech. 2020, 44(8):1200-1218.

Zhu HP, Zhou ZY, Yang RY, Yu AB. Discrete particle simulation of particulate systems: theoretical developments. Chemical Engineering Science. 2007, 62, 3378-3396.

Zhao J, Shan T. Coupled CFD-DEM simulation of fluid-particle interaction in geomechanics. Powder Technol. 2013, 239, 248-258.

Zhang F, Li ML, Peng M, Chen C. Zhang LM. Three-dimensional DEM modeling of the stress-strain behavior for the gap-graded soils subjected to internal erosion. Acta Geotechnica. 2018, 14(66), 1-17.

Zhou ZY, Kuang SB, Chu KW, Yu AB. Discrete particle simulation of particle-fluid flow: model formulations and their applicability. Journal of Fluid Mechanics. 2010, 661, 482-510.

Caption of Tables

Table 1 Simulation program

Table 2 Summary of model parameters

Table 3 Number of simulated particles and micromechanical properties of each sample

Table 1 Simulation program

Simulation identity	Fines content, F_c (%)	Confining pressure, p' (kPa)	Hydraulic gradient, i
FC20P50-IL	20	50	0.2
FC20P200-IL	20	200	0.2
FC35P50-IL	35	50	0.2
FC35P200-IL	35	200	0.2
FC20P50	20	50	2
FC20P100	20	100	2
FC20P200	20	200	2
FC25P50	25	50	2
FC25P100	25	100	2
FC25-P200	25	200	2
FC30P50	30	50	2
FC30P100	30	100	2
FC30P200	30	200	2
FC35P50	35	50	2
FC35P100	35	100	2
FC35P200	35	200	2

Table 2 Summary of model parameters

Model parameters		
Physical model	Sample dimensions $L \times W \times H$ (mm)	15×15×15
	Simulation time (s)	14.0
CFD	Cells	5×5×6
	Fluid viscosity, μ (Pa s)	1×10^{-3}
	Density, ρ_f (kg/m^3)	1000
DEM	Elastic modulus, E (GPa)	7
	Poisson's ratio, v	0.3
	Coefficient of Restitution, e	0.7
	Friction coefficient, μ_f	0.5
	Rolling friction coefficient, μ_r	0.1

Table 3 Number of simulated particles and micromechanical properties of each sample

Simulation identity	Fines content (%)	No. of total particles	No. of coarse particles	No. of fine particles	Void ratio, e	Relative density, R_d (%)
FC20P50	20	9926	587	9339	0.46	58.8
FC20P100	20	9944	587	9357	0.46	58.8
FC20P200	20	9968	587	9381	0.46	58.8
FC25P50	25	9902	447	9455	0.44	62.4
FC25P100	25	9931	447	9484	0.44	62.4
FC25P200	25	9953	447	9506	0.44	62.4
FC30P50	30	9846	351	9495	0.42	66.1
FC30P100	30	9906	351	9555	0.42	66.1
FC30P200	30	9972	351	9621	0.42	66.1
FC35P50	35	9845	280	9565	0.41	70.2
FC35P100	35	9904	280	9624	0.41	70.2
FC35P200	35	9951	280	9671	0.41	70.2

Caption of Figures

Figure 1 (a) Illustration of internal erosion; (b) schematic diagram of coarse grid DEM-CFD simulation approach adopted in this study

Figure 2 (a) Comparison of the CFD-DEM prediction and the analytical solution for velocity of single particle settling in water; (b) initial configuration of model; (c) displacements of top particle for input velocity of 0.005 m/s; (d) calculated displacement under gravity and particle-fluid forces from initial tentative configuration

Figure 3 Particle size distributions of gap graded samples analyzed in this study

Figure 4 Variation of void ratio with fines content

Figure 5 Coupled DEM-CFD simulation for internal erosion (Particles are colored by radius and the CFD grid is overlain in blue)

Figure 6 Simulation results for the samples with F_c=20% and 35% under i=0.2 and p'=50 and 200 kPa: (a) cumulative eroded soil weight percentage; (b) axial strain; (c) radial strain

Figure 7 Cumulative eroded mass percentage for the sample with: (a) F_c=20% and 35%; (b) F_c=25% and 30% under i=2.0 and p'=50 and 200 kPa

Figure 8 (a) Axial strain and (b) radial strain for the samples with F_c= 30% and 35%; (c) axial strain and (b) radial strain for the samples with F_c= 20% and 25% under i=2 and p'=50 and 200 kPa

Figure 9 Vertical profile of fines content for the samples with F_c=20% and 35% before and after erosion

Figure 10 Initial profile, contact force chain and normal strain energy of local packing for the sample with (a) F_c=35% and p'=50 kPa; (b) F_c=35% and p'=200 kPa.

Figure 11 Initial profile, contact force chain and normal strain energy of local packing for the sample with (a) F_c=20% and p'=50 kPa; (b) F_c=20% and p'=200 kPa.

Figure 12 Characteristics of the force chain networks for the samples with different F_c=35% and p'=50 kPa: (a) network contribution of confining pressure; (b) fraction of different force chain networks (The fraction of the weak force chain networks formed by overall particles and fine particles is coincide)

Figure 13 Characteristics of erosion for the samples with different F_c=20% and p'=50 kPa: (a) network contribution of confining pressure; (b) fraction of different force chain networks

Figure 14 The evolution of local packings during erosion for samples with F_c=35%: (a) initial configuration; (b) before turning point; (c) after turning point

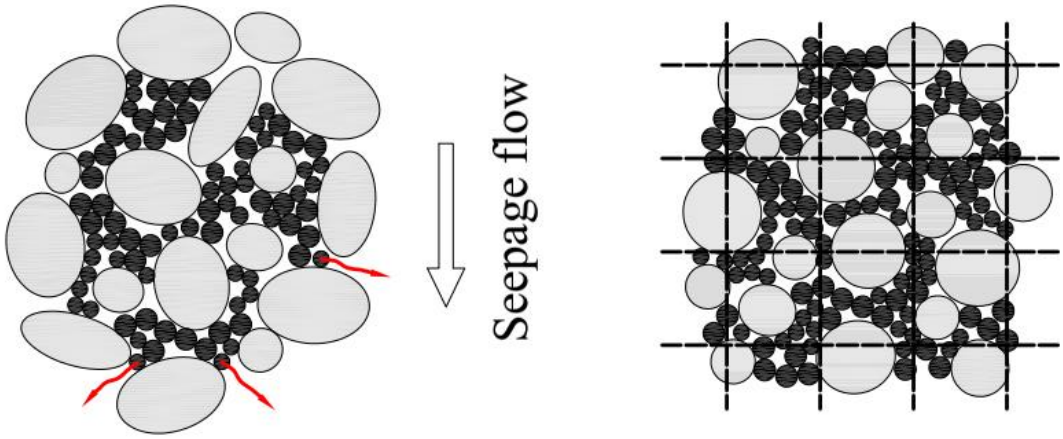

Figure 1 (a) Illustration of internal erosion; (b) schematic diagram of coarse grid DEM-CFD simulation approach adopted in this study

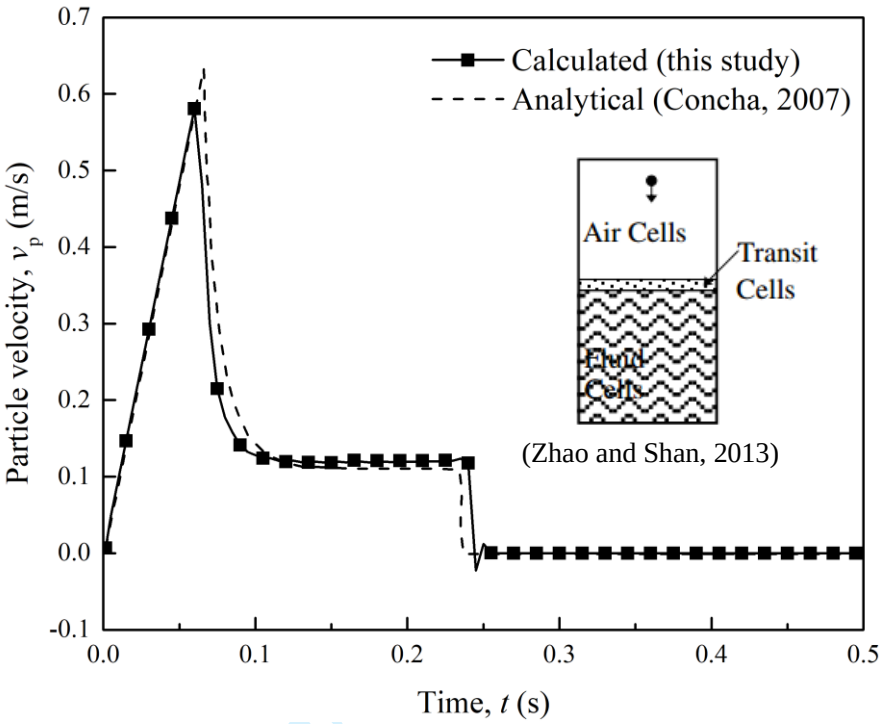
Calculated (this study)
Analytical (Concha, 2007)
Air Cells
Transit Cells
Fluid Cells
(Zhao and Shan, 2013)
Particle velocity, v_p (m/s)
Time, t (s)
0.7
0.6
0.5
0.4
0.3
0.2
0.1
0.0
-0.1
0.0
0.1
0.2
0.3
0.4
0.5

(a)

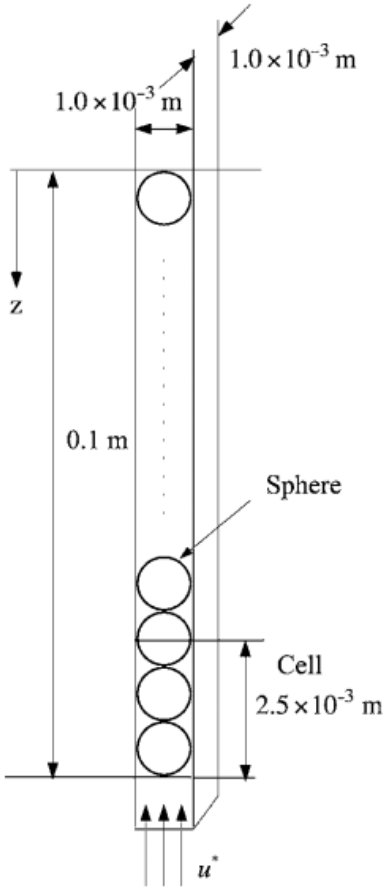
1.0×10^{-3} m
1.0×10^{-3} m
z
0.1 m
Sphere
Cell
2.5×10^{-3} m
u^*

(b)

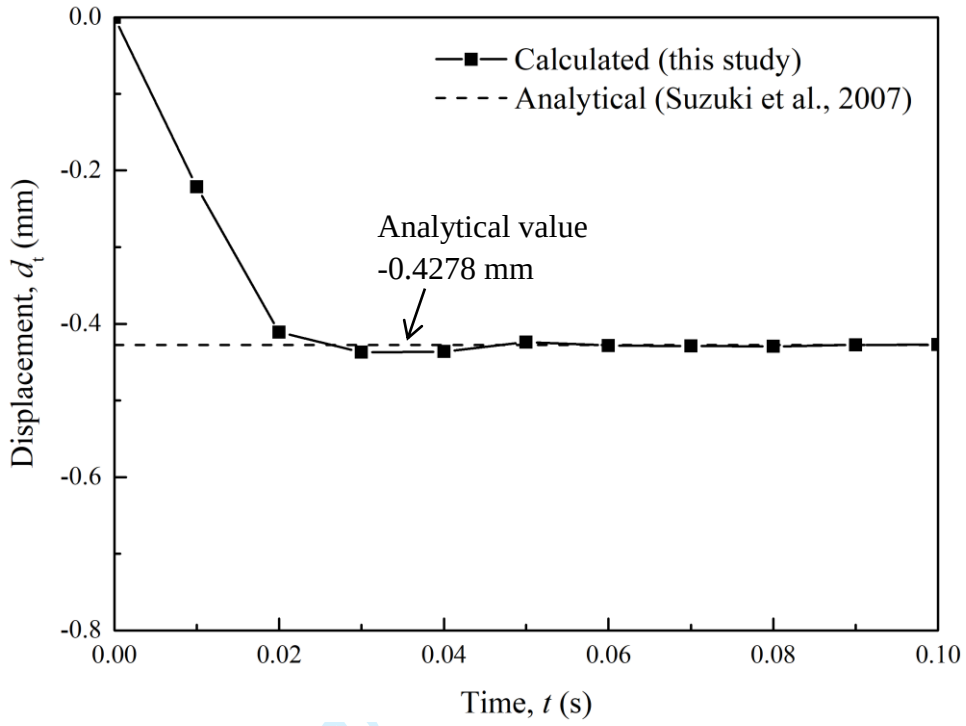

(c)

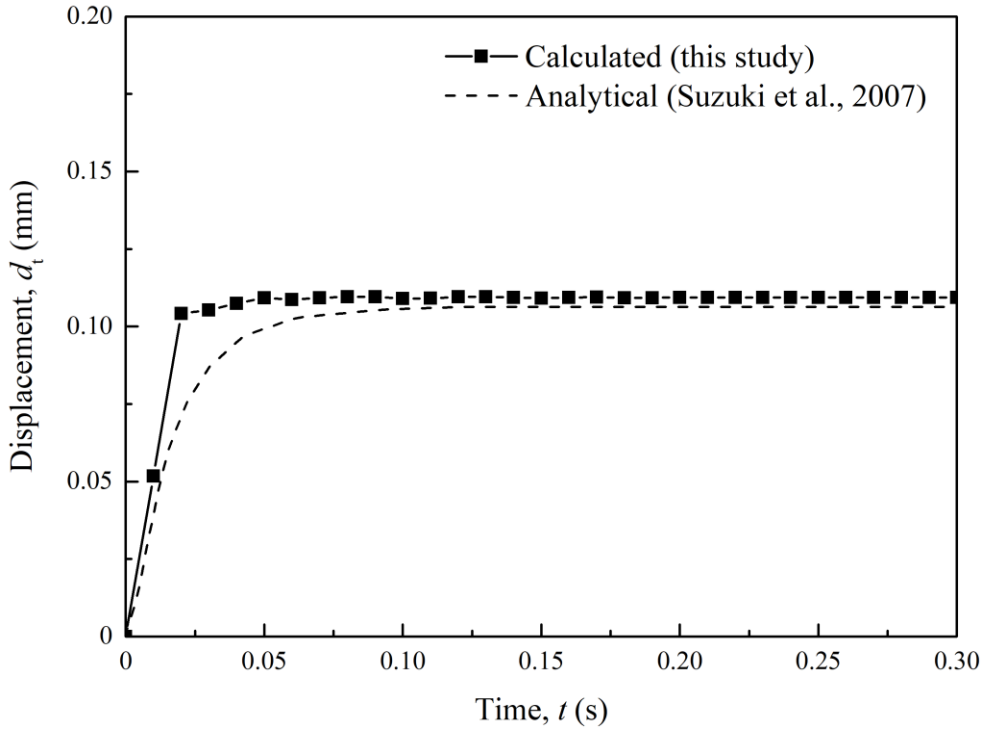

(d)

Figure 2 (a) Comparison of the CFD-DEM prediction and the analytical solution for velocity of single particle settling in water; (b) initial configuration of model (Suzuki et al., 2007); (c) displacements of top particle for input velocity of 0.005 m/s; (d) calculated displacement under gravity and particle-fluid forces from initial tentative configuration

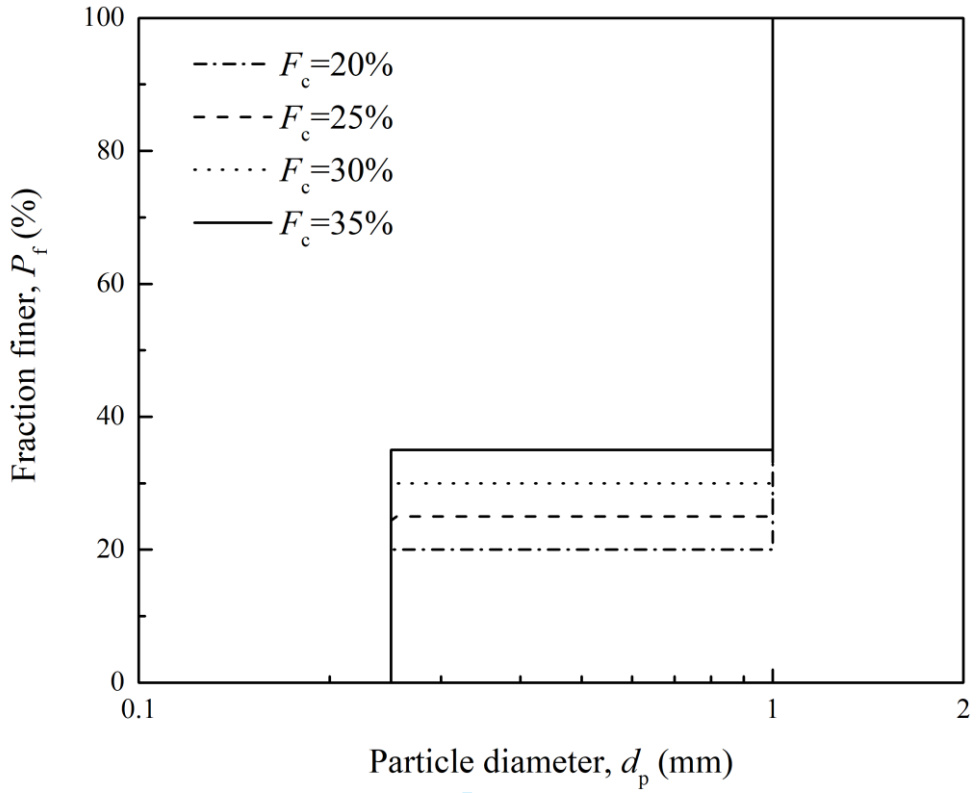

Figure 3 Particle size distributions of gap graded samples analyzed in this study

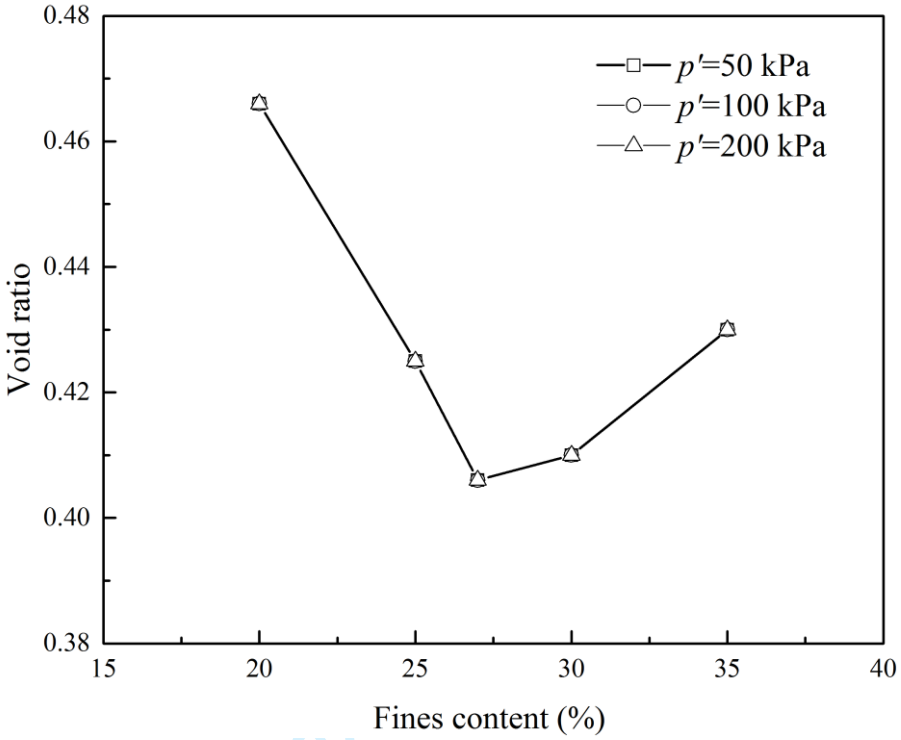

Figure 4 Variation of void ratio with fines content

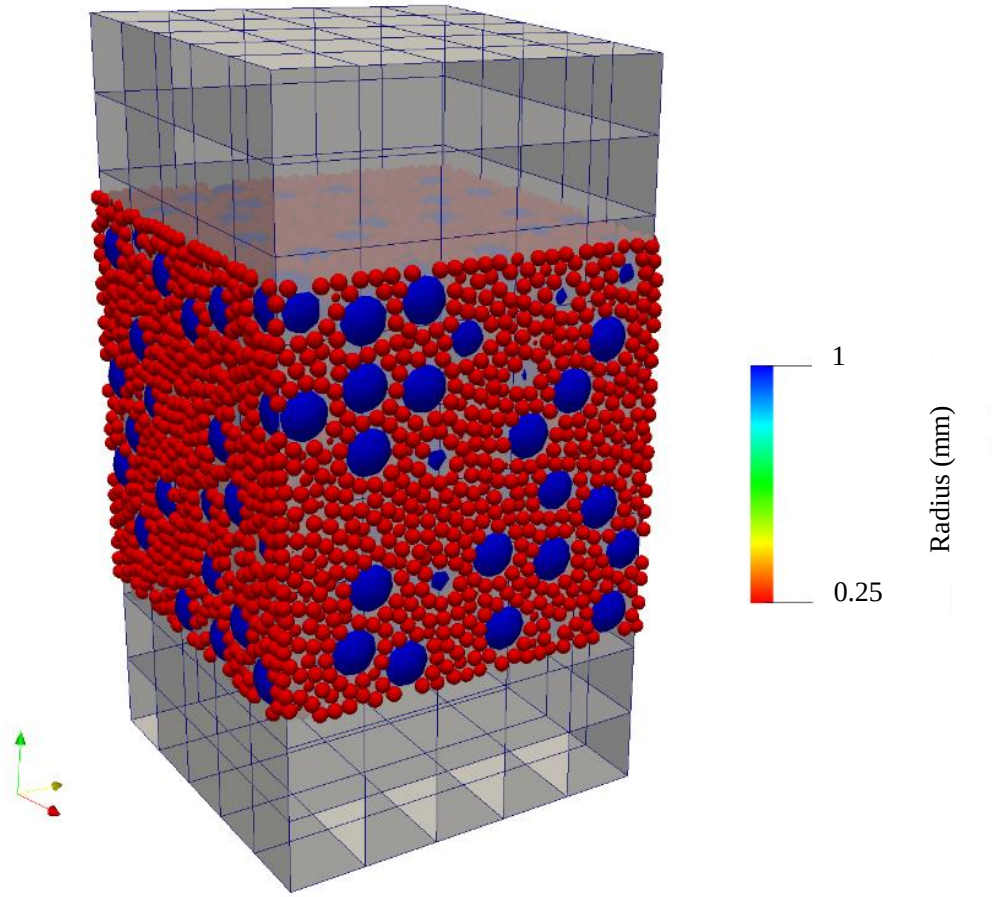

Figure 5 Coupled DEM-CFD simulation for internal erosion (Particles are colored by radius and the CFD grid is overlain in blue)

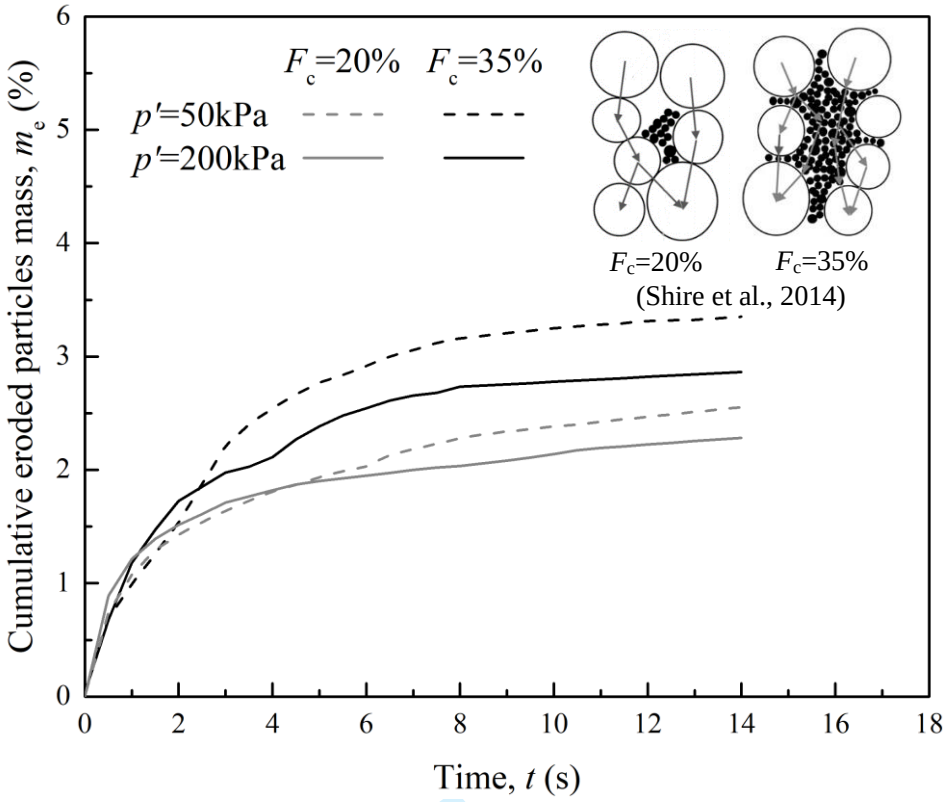
F_c=20% F_c=35%
p'=50kPa
p'=200kPa
F_c=20%
F_c=35%
(Shire et al., 2014)
Cumulative eroded particles mass, m_e (%)
Time, t (s)

(a)

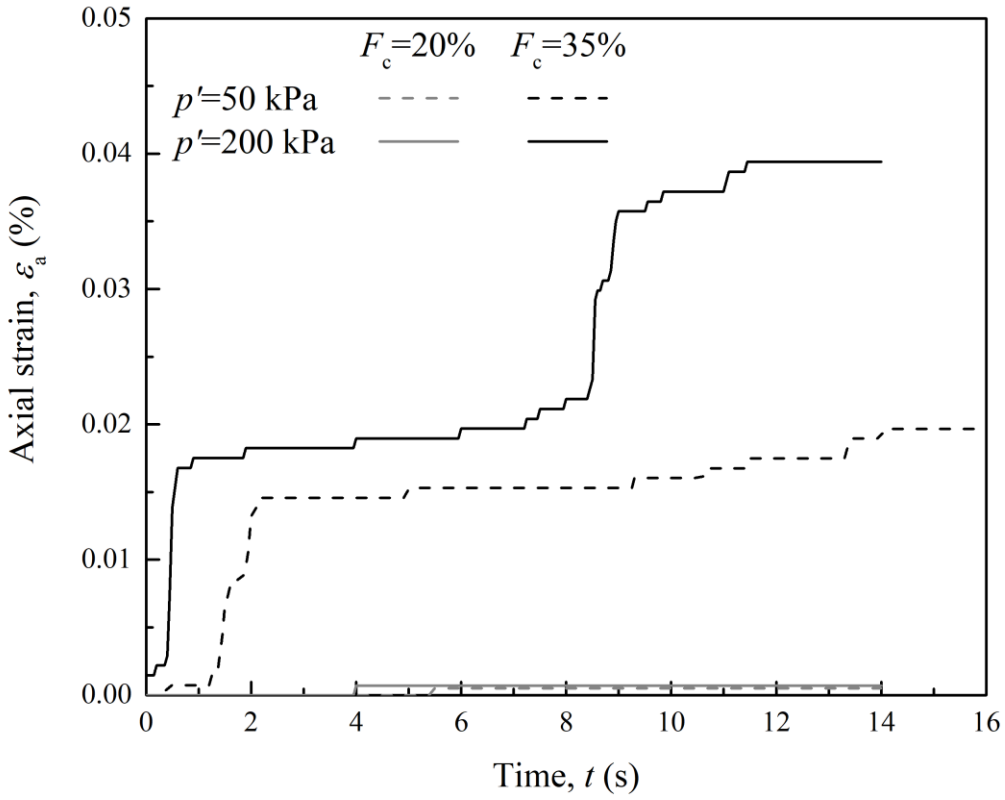
F_c=20% F_c=35%
p'=50 kPa
p'=200 kPa
Axial strain, ε_a (%)
Time, t (s)

(b)

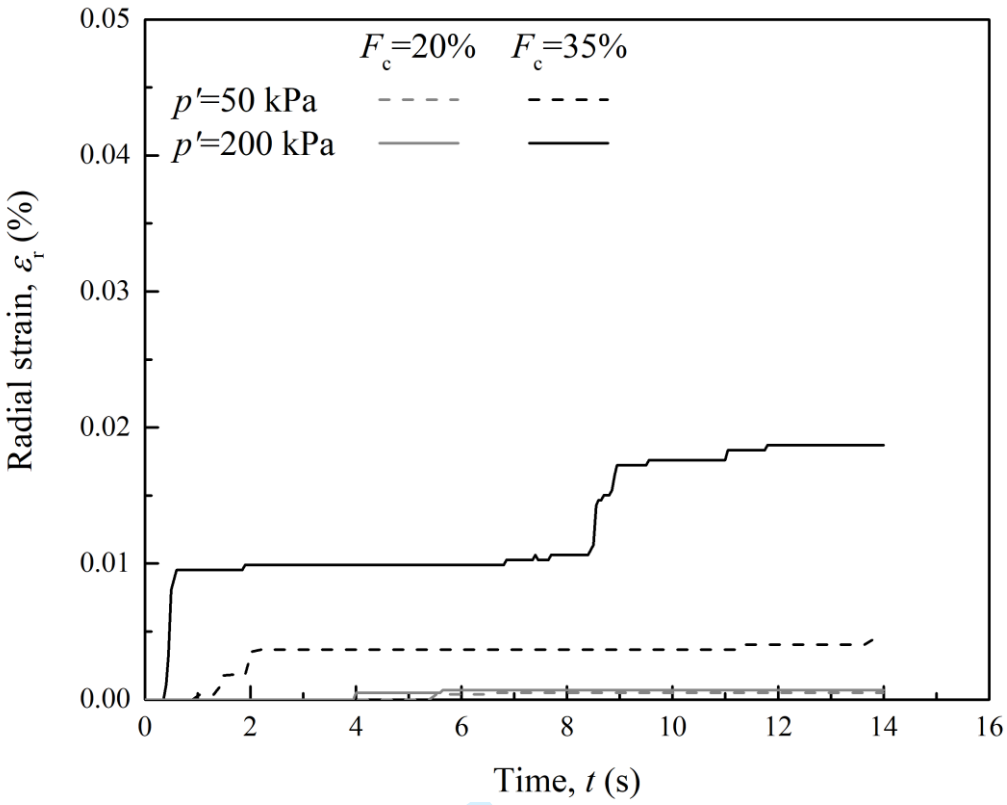

(c)

Figure 6 Simulation results for the samples with F_c=20% and 35% under i=0.2 and p'=50 and 200 kPa: (a) cumulative eroded soil weight percentage; (b) axial strain; (c) radial strain

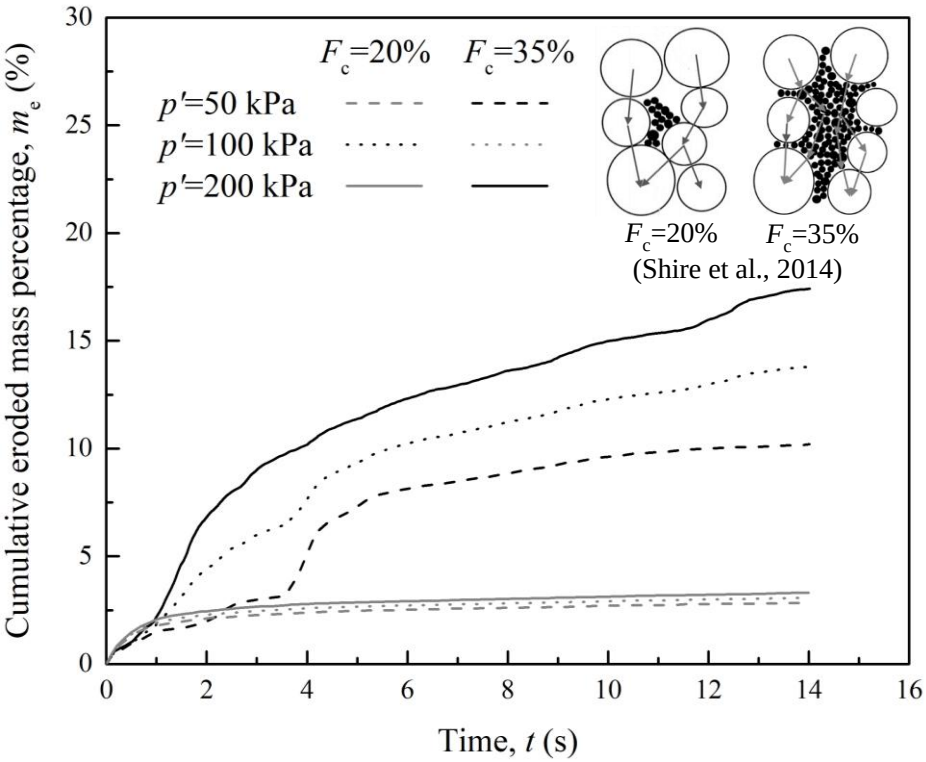

(a)

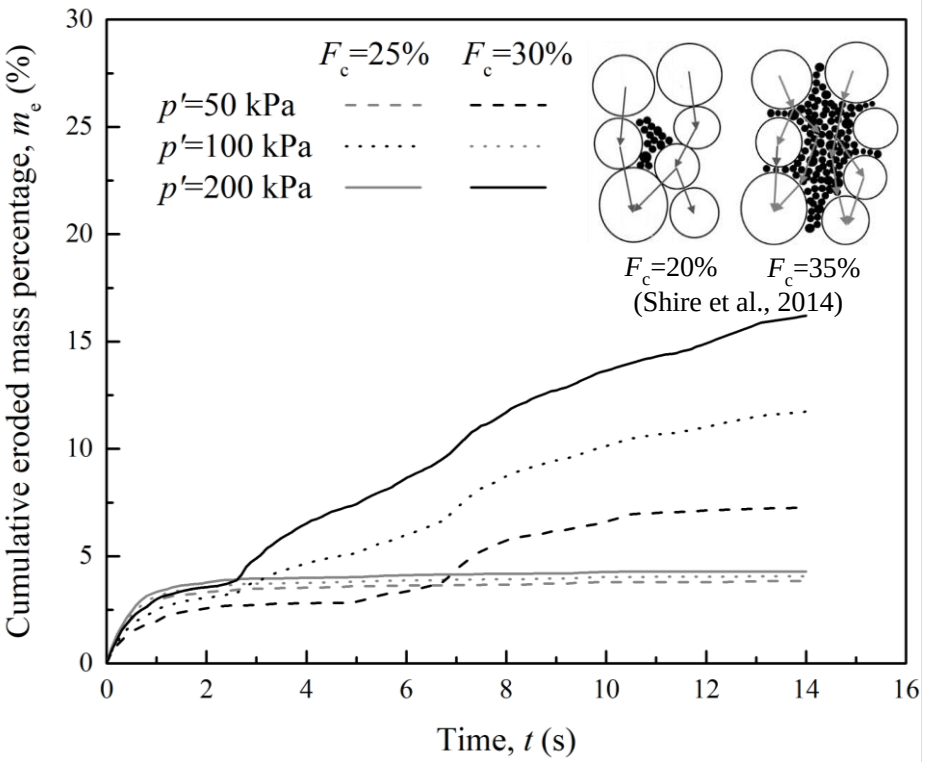

(b)

Figure 7 Cumulative eroded mass percentage for the sample with: (a) F_c=20% and 35%; (b) F_c=25% and 30% under i=2.0 and p'=50 and 200 kPa

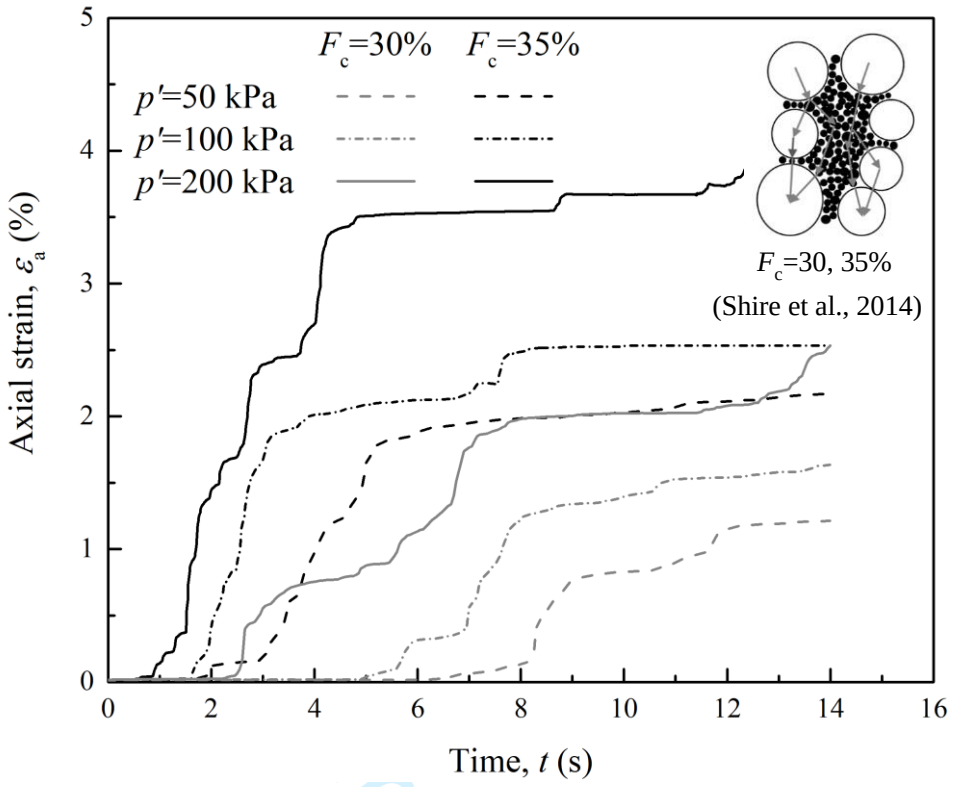
F_c=30% F_c=35%
p'=50 kPa
p'=100 kPa
p'=200 kPa
F_c=30, 35%
(Shire et al., 2014)
Axial strain, ε_a (%)
Time, t (s)

(a)

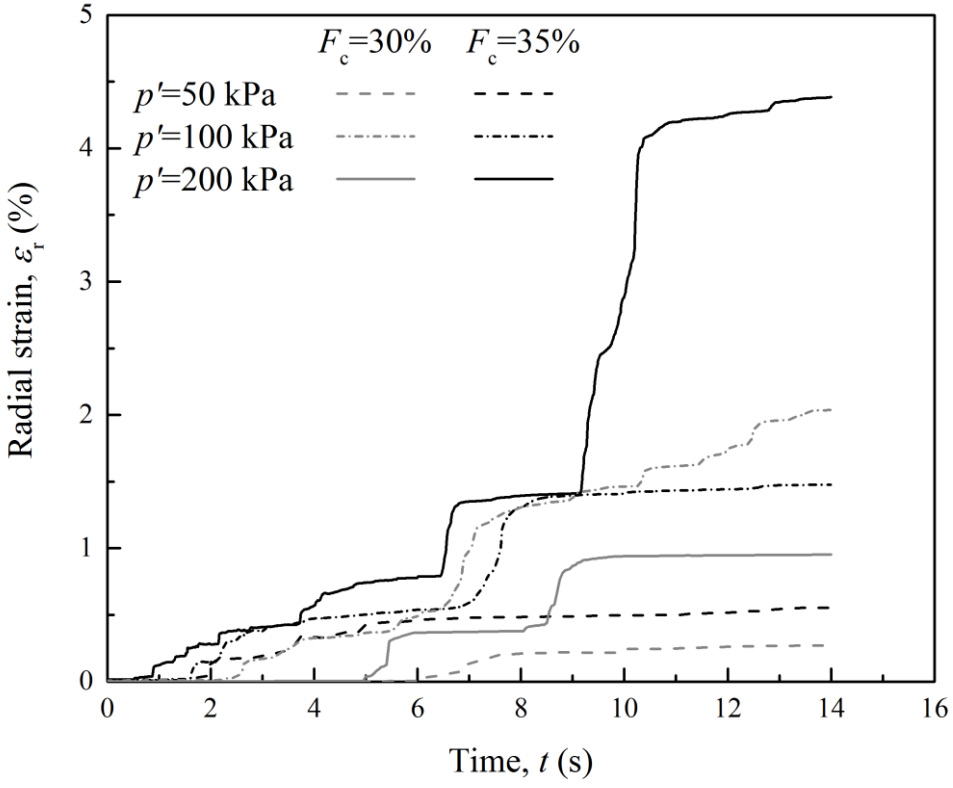
F_c=30% F_c=35%
p'=50 kPa
p'=100 kPa
p'=200 kPa
Radial strain, ε_r (%)
Time, t (s)

(b)

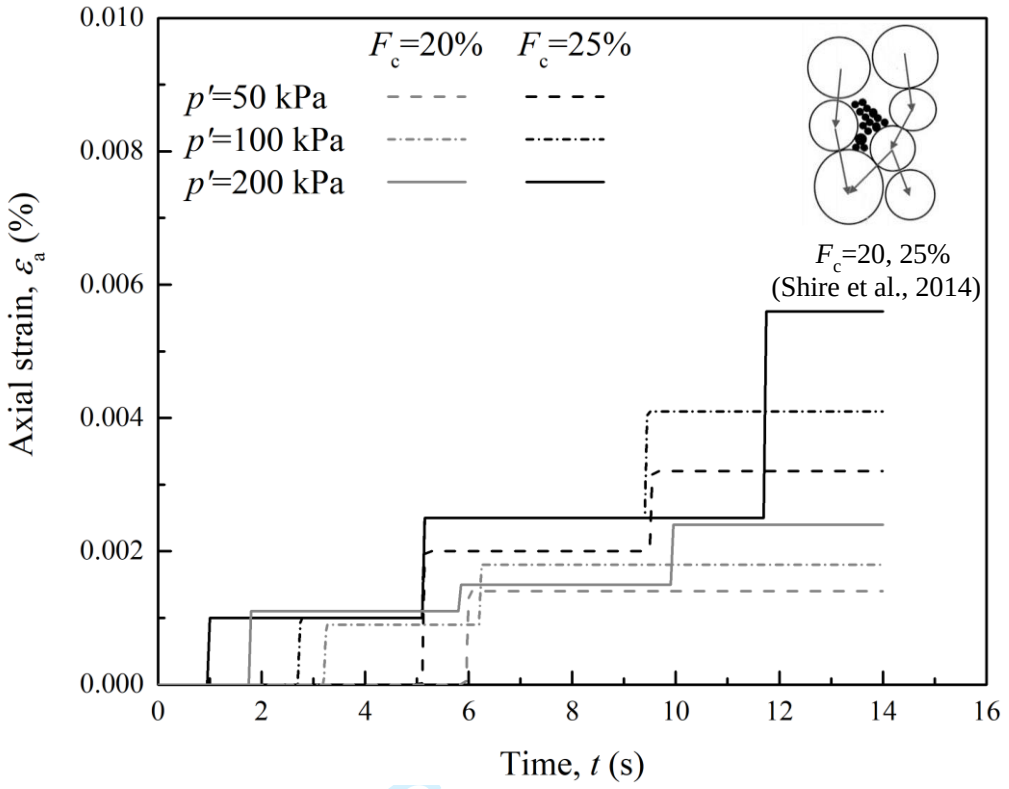

(c)

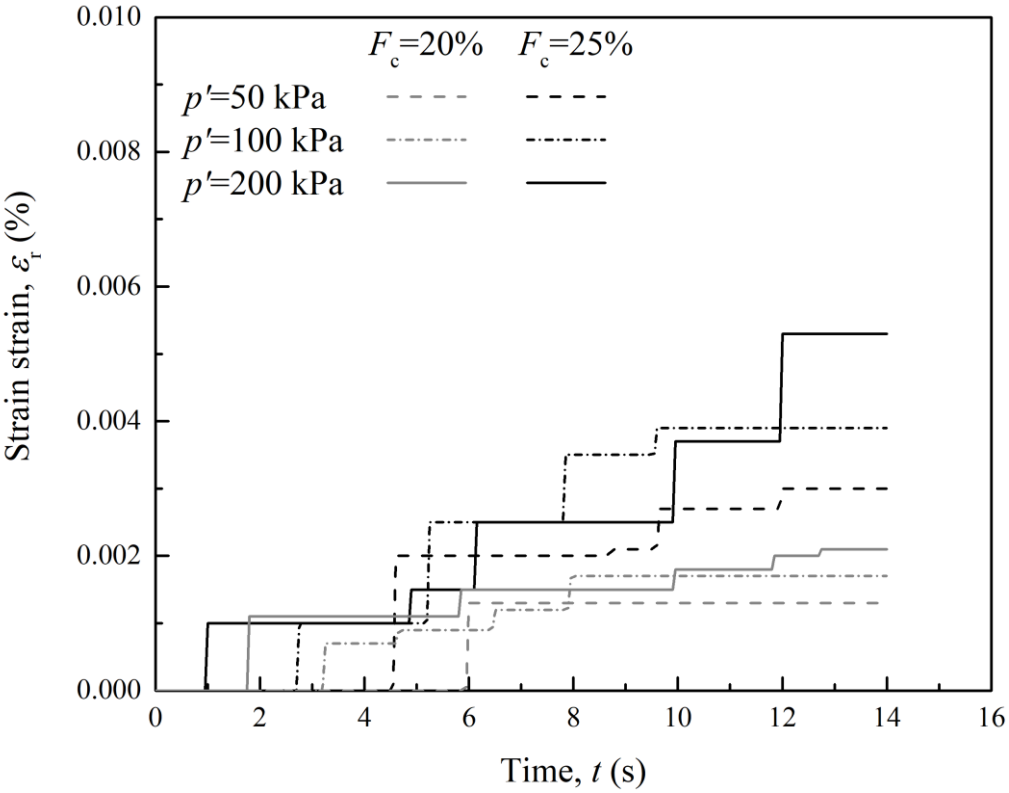

(d)

Figure 8 (a) Axial strain and (b) radial strain for the samples with F_c= 30% and 35%; (c) axial strain and (b) radial strain for the samples with F_c= 20% and 25% under i=2 and p'=50 and 200 kPa

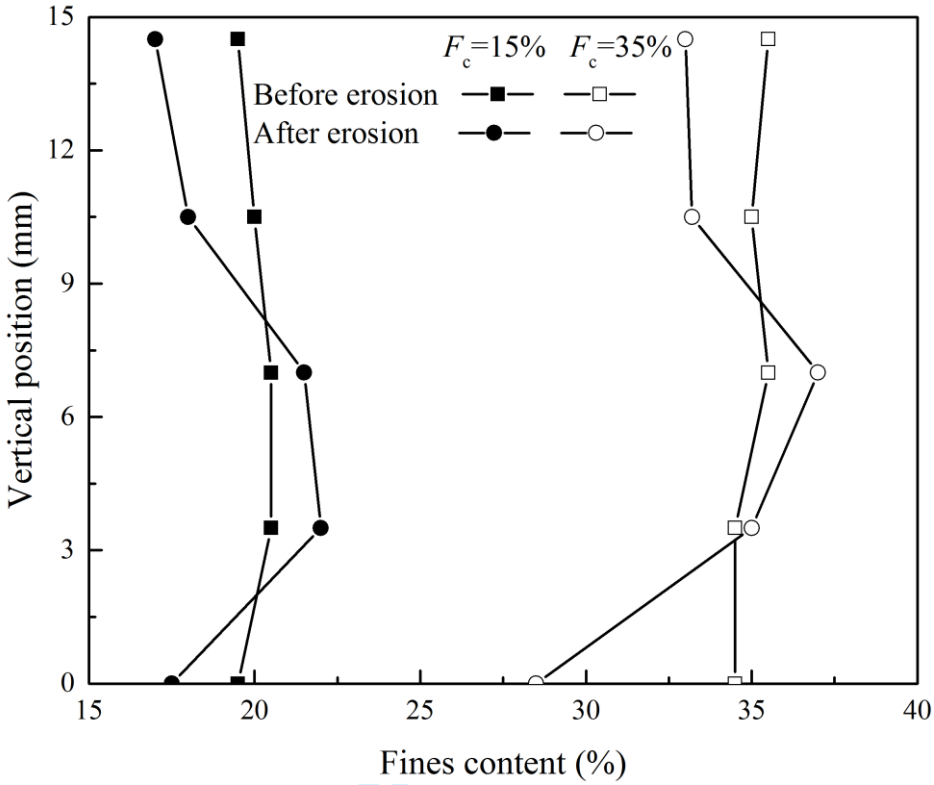

Figure 9 Vertical profile of fines content for the samples with Fc=20% and 35% before and after erosion

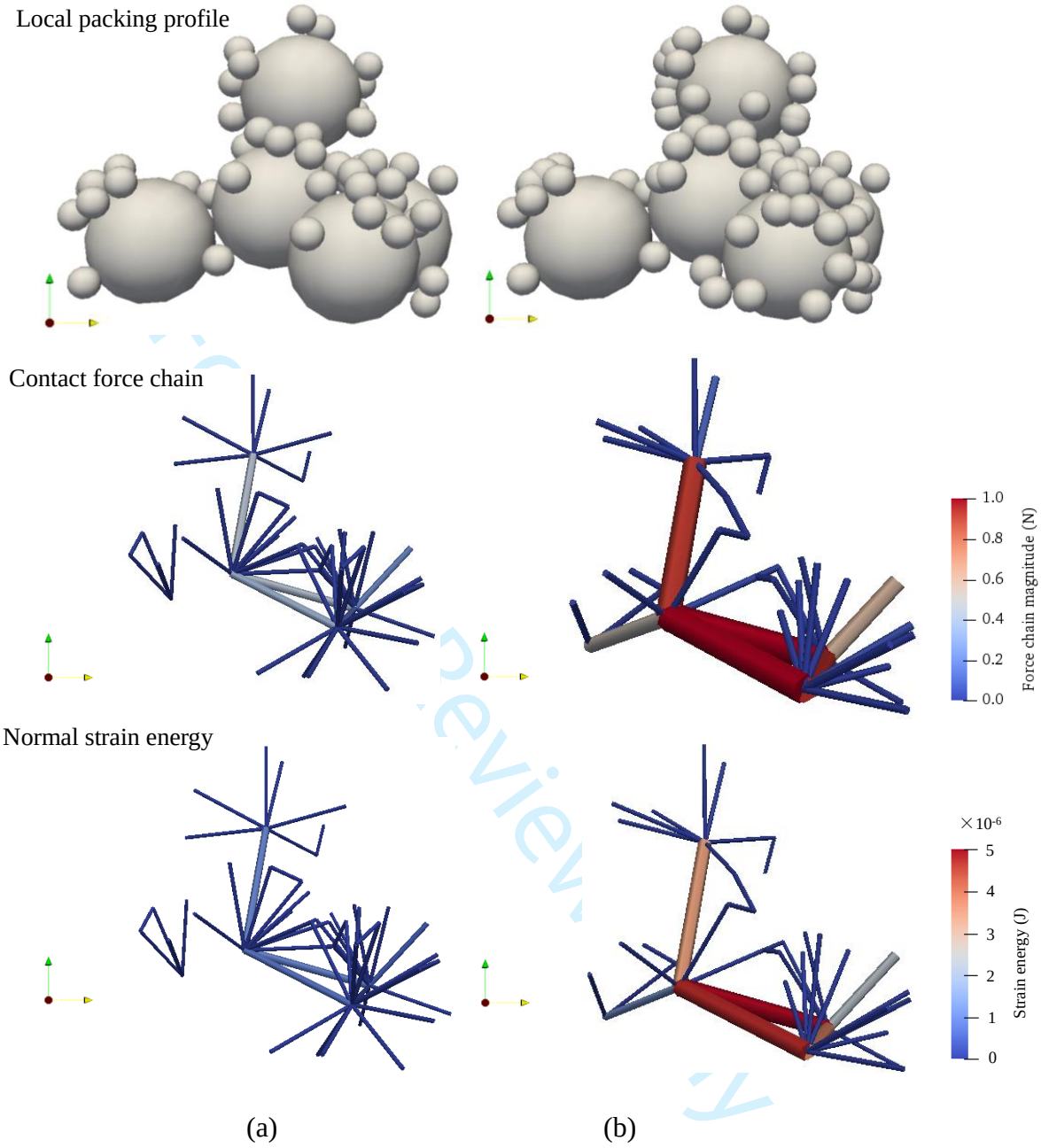

Figure 10 Initial profile, contact force chain and normal strain energy of local packing for the sample with (a) F_c=20% and p'=50 kPa; (b) F_c=20% and p'=200 kPa.

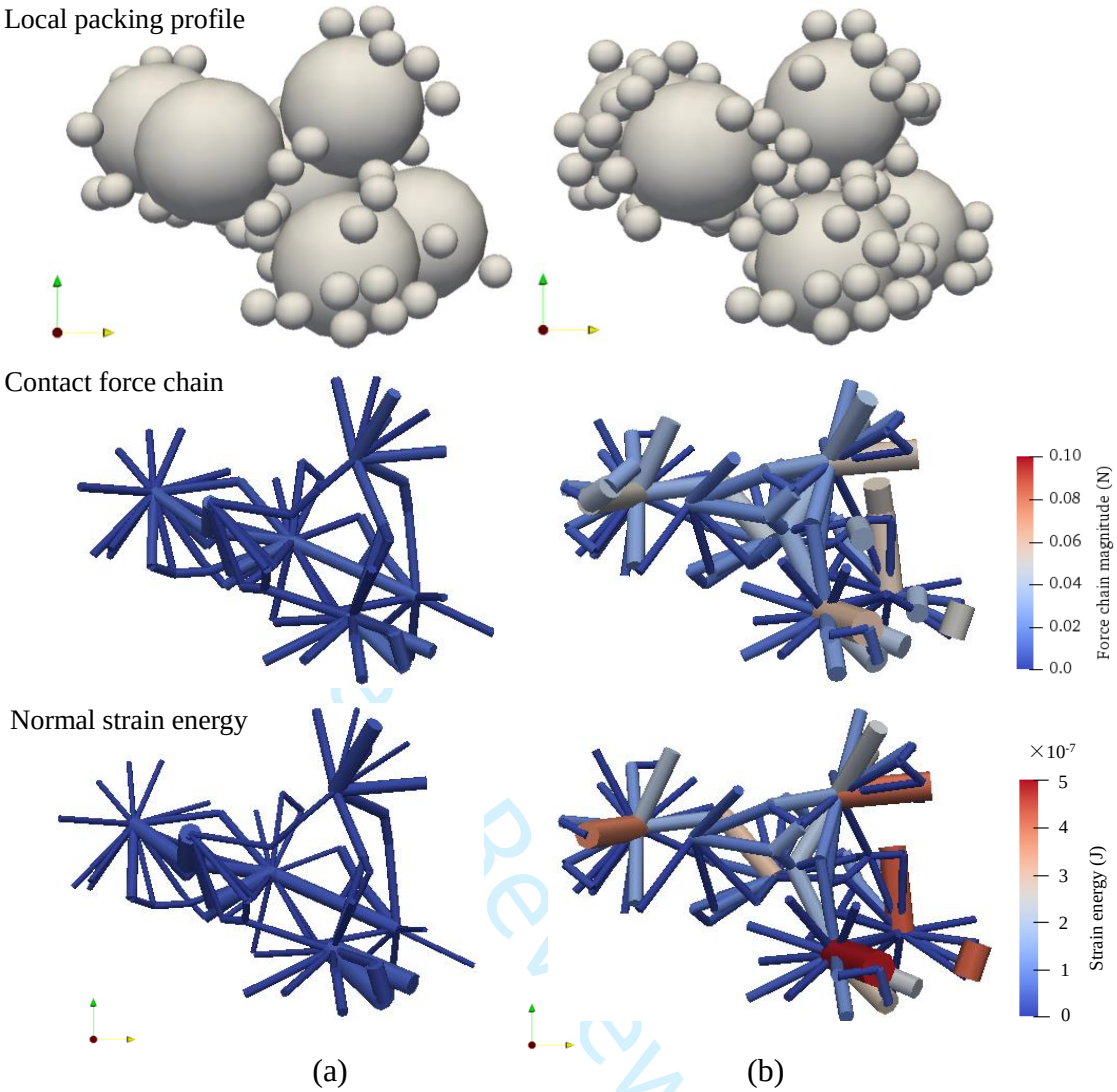

Figure 11 Initial profile, contact force chain and normal strain energy of local packing for the sample with (a) F_c=35% and p'=50 kPa; (b) F_c=35% and p'=200 kPa.

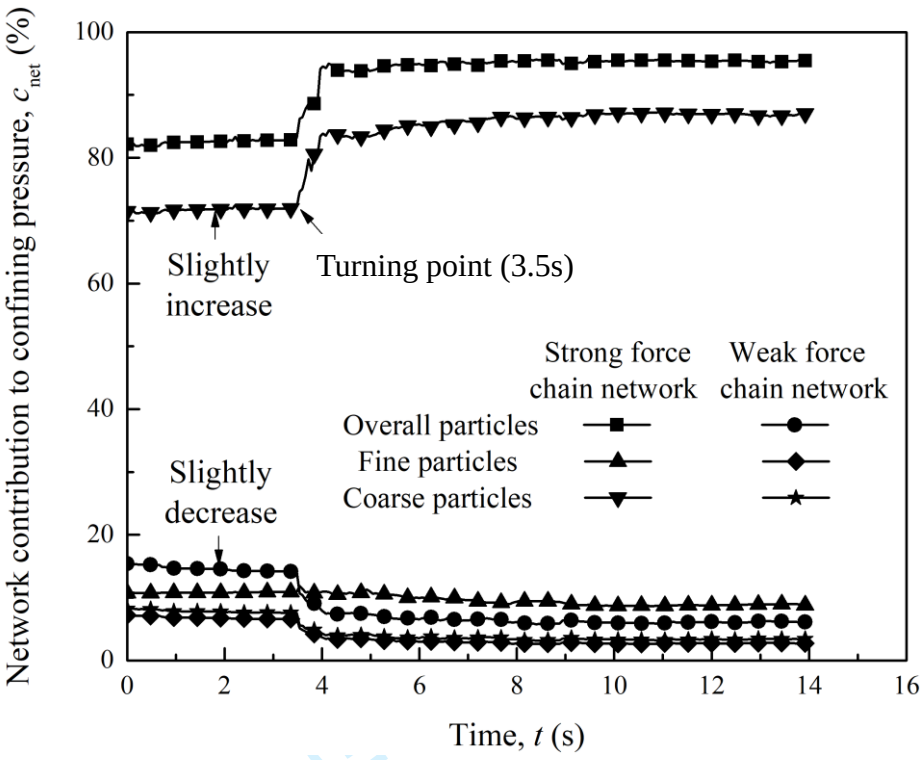

(a)

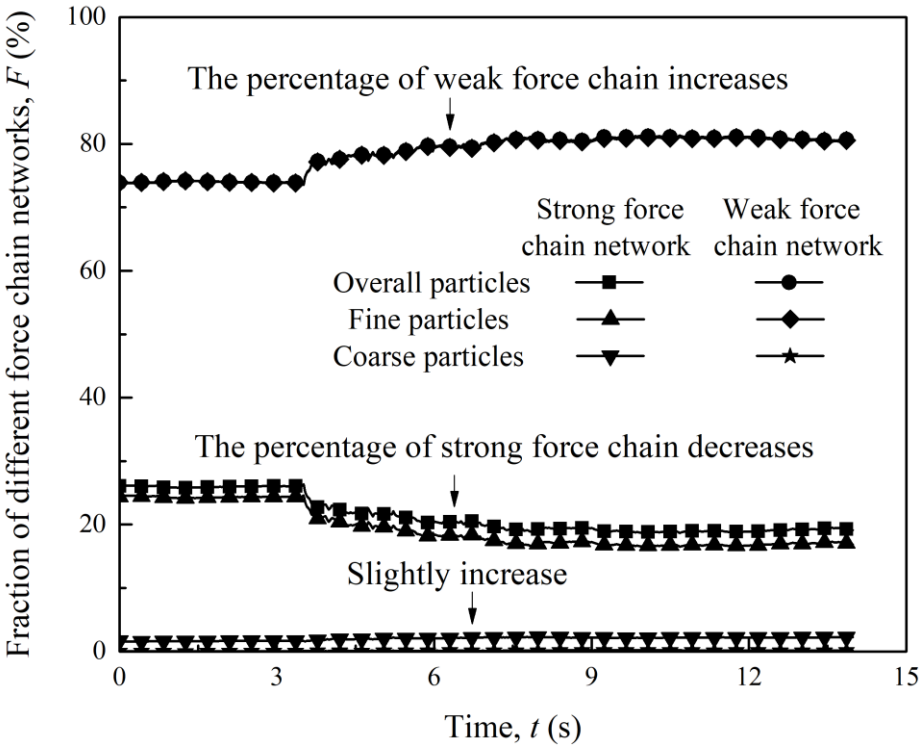

(b)

Figure 12 Characteristics of the force chain networks for the samples with different F_c=35% and p'=50 kPa: (a) network contribution of confining pressure; (b) fraction of different force chain networks (The fraction of the weak force chain networks formed by overall particles and fine particles is coincide)

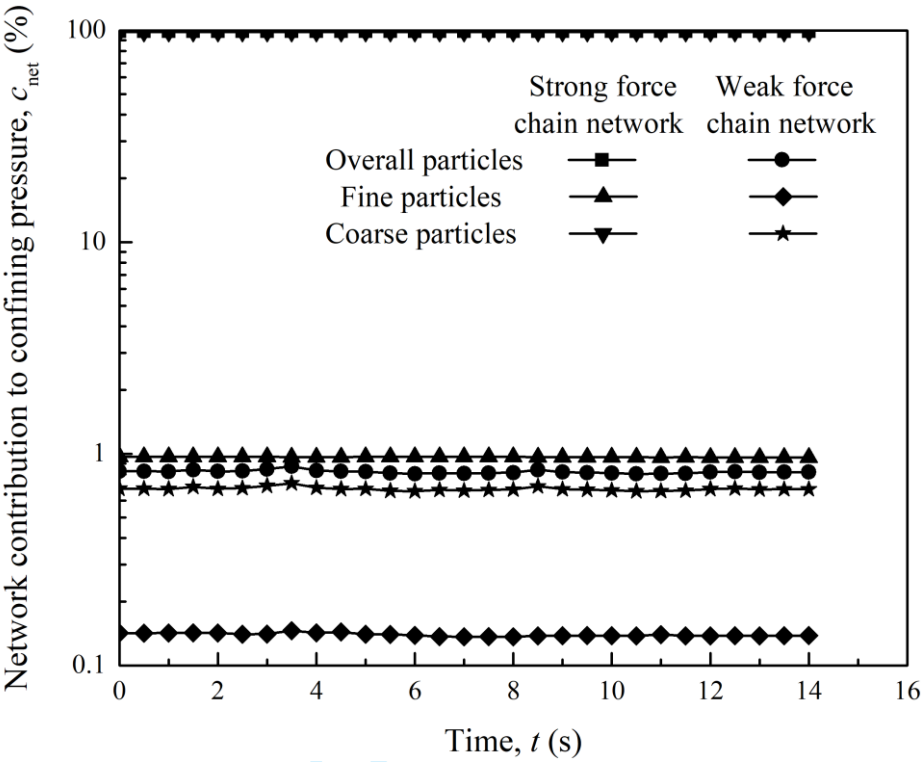

(a)

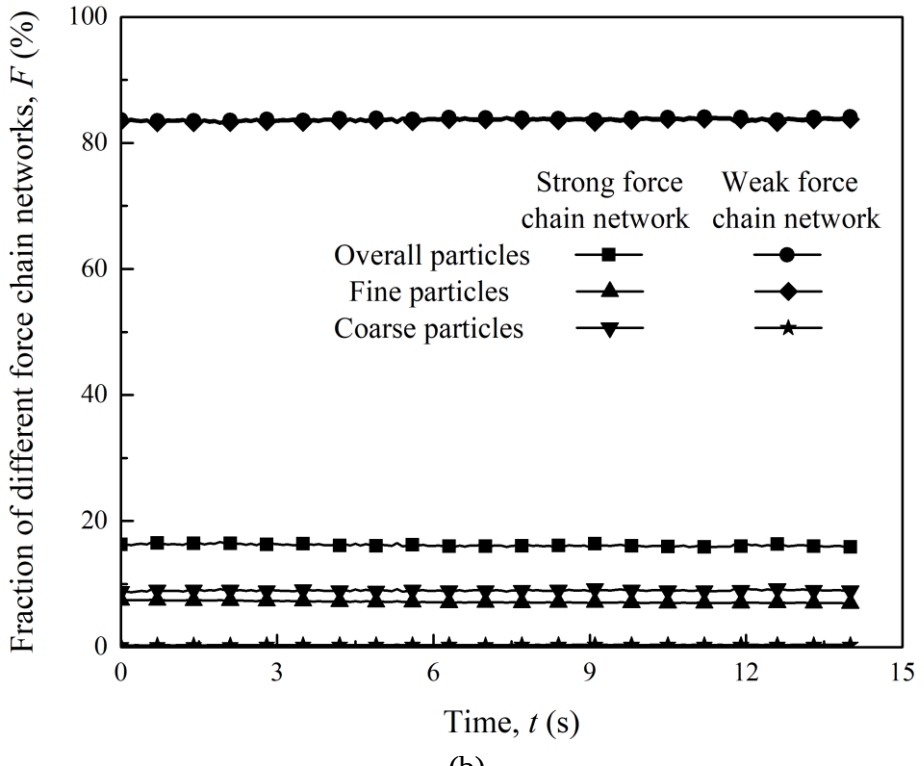

(b)

Figure 13 Characteristics of erosion for the samples with different F_c=20% and p'=50 kPa: (a) network contribution of confining pressure; (b) fraction of different force chain networks

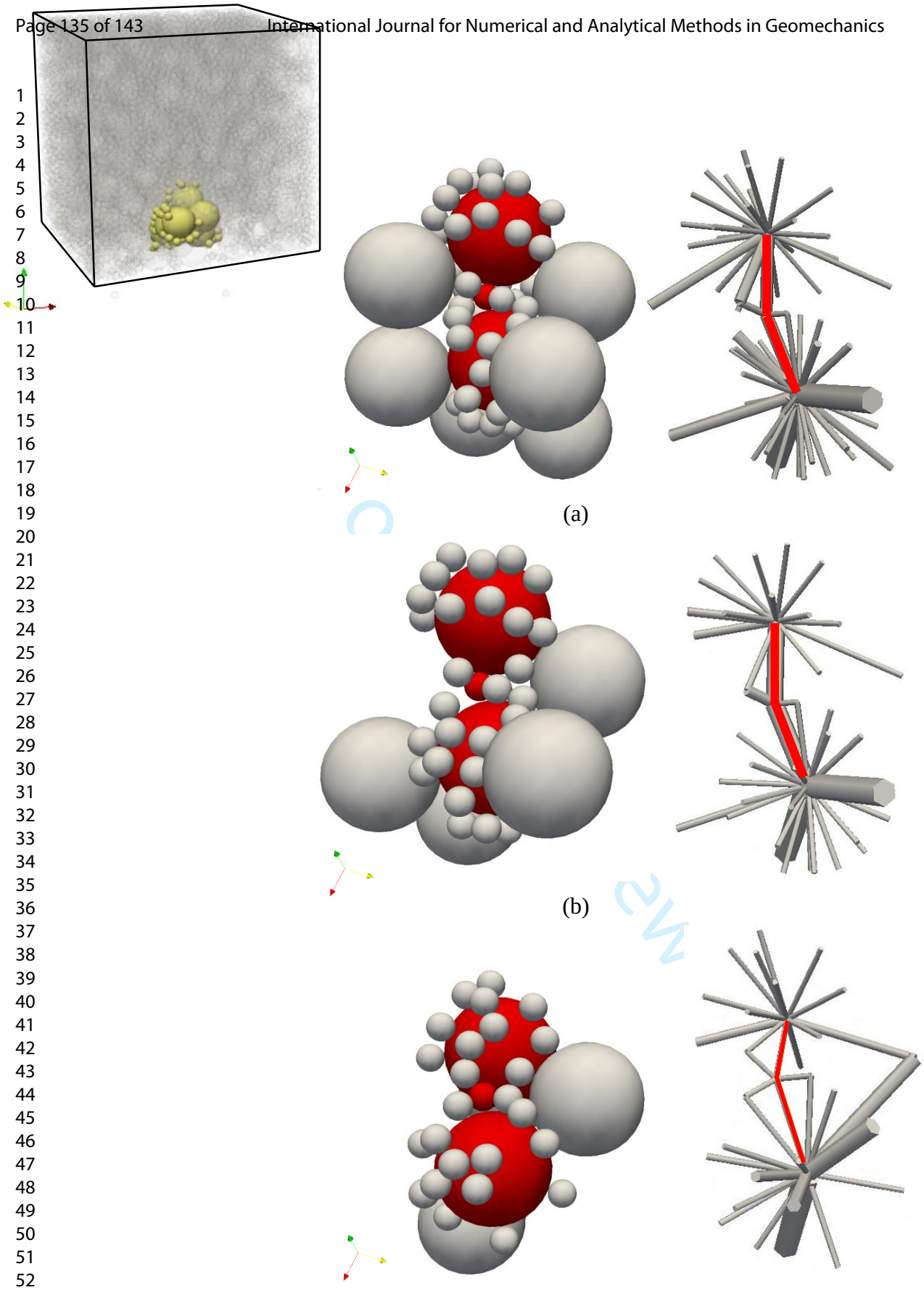

(a)

(b)

(c)

Figure 14 The evolution of local packings during erosion for samples with F_c=35%: (a) initial configuration; (b) before turning point; (c) after turning point (The thickness of the lines represents the magnitude of contact force)

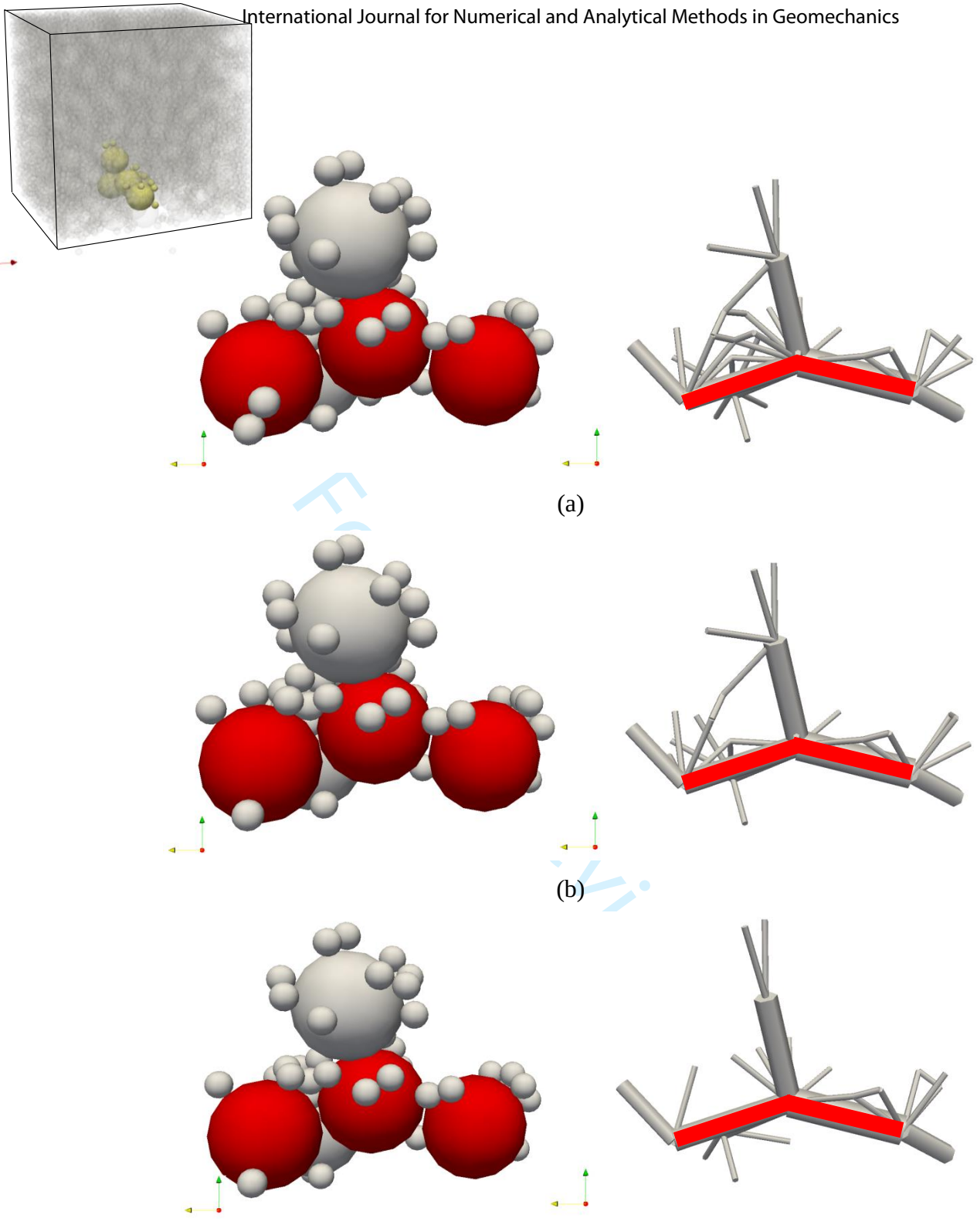

Figure 15 The evolution of local packings during erosion for samples with F_c=20%: (a) initial configuration; (b) before turning point; (c) after turning point (The thickness of the lines represents the magnitude of contact force)

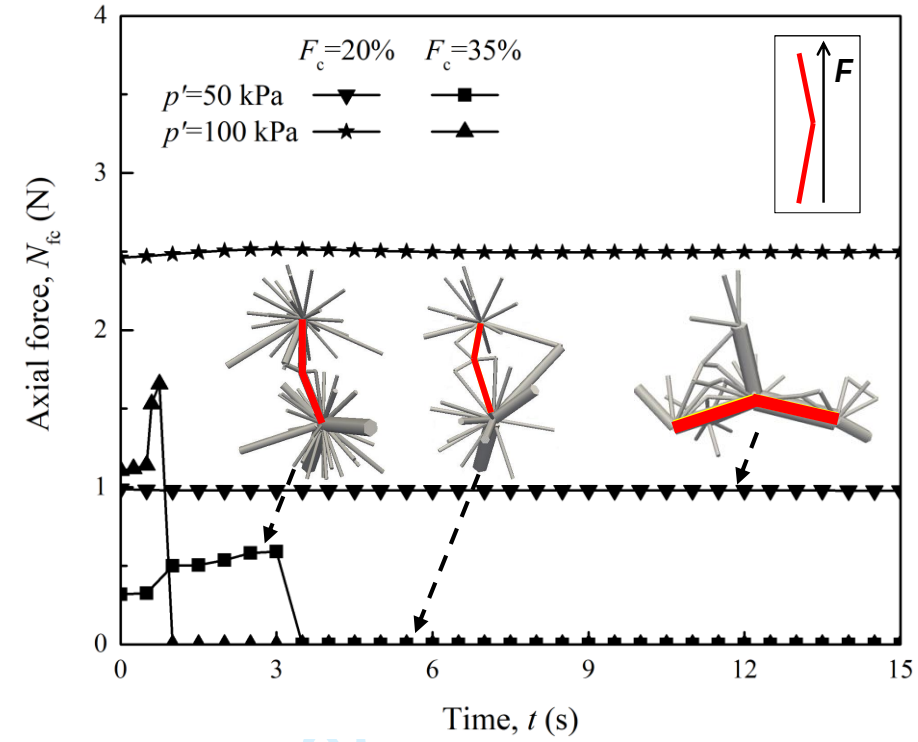

(a)

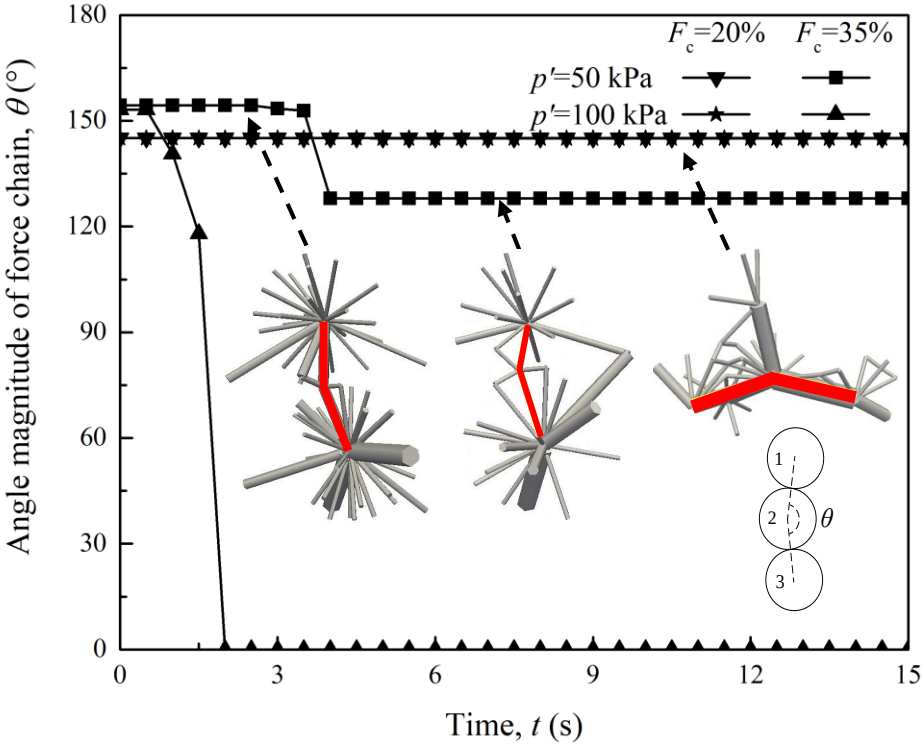

(b)

Figure 16 Evolution of (a) axial force and (b) angle magnitude for a typical force chain in samples with different F_c (20% and 35%) and p' (50 kPa and 200 kPa) (Angle of 0° means that the contact is separated)

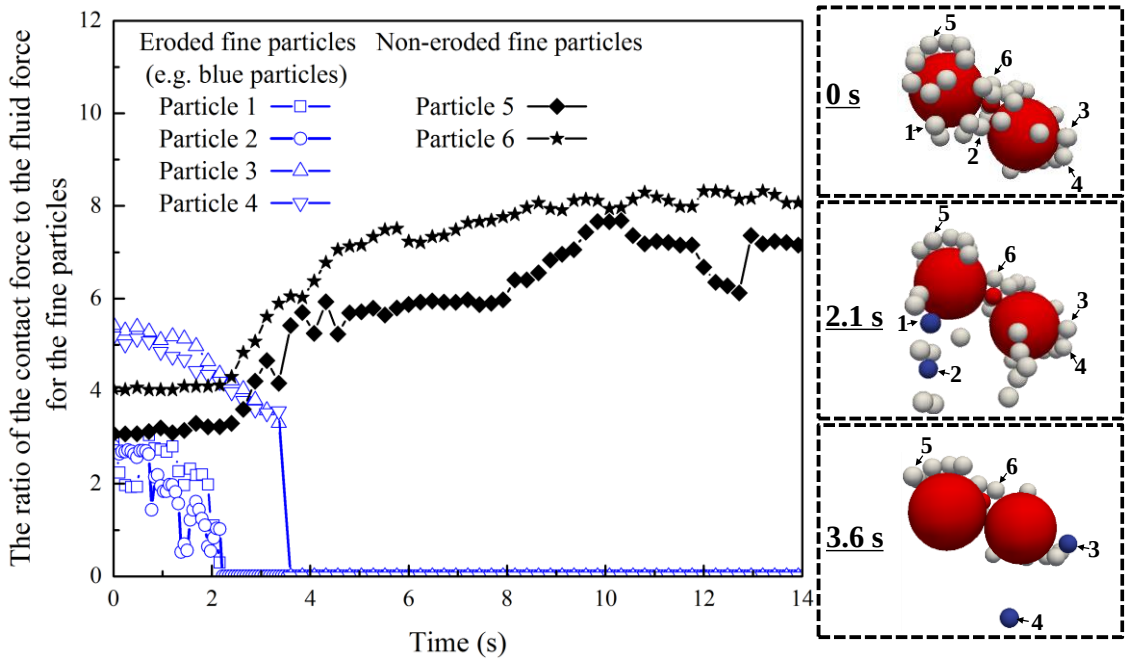

Note: The red particles denote the chained particles. The blue and gray particles represent eroded and non-eroded fine particles at the moment of interests, respectively.

Figure 17 Evolution of the ratio of the average contact force to the fluid force for the fine particles in a local packing (F_c=35%, p'=50 kPa)

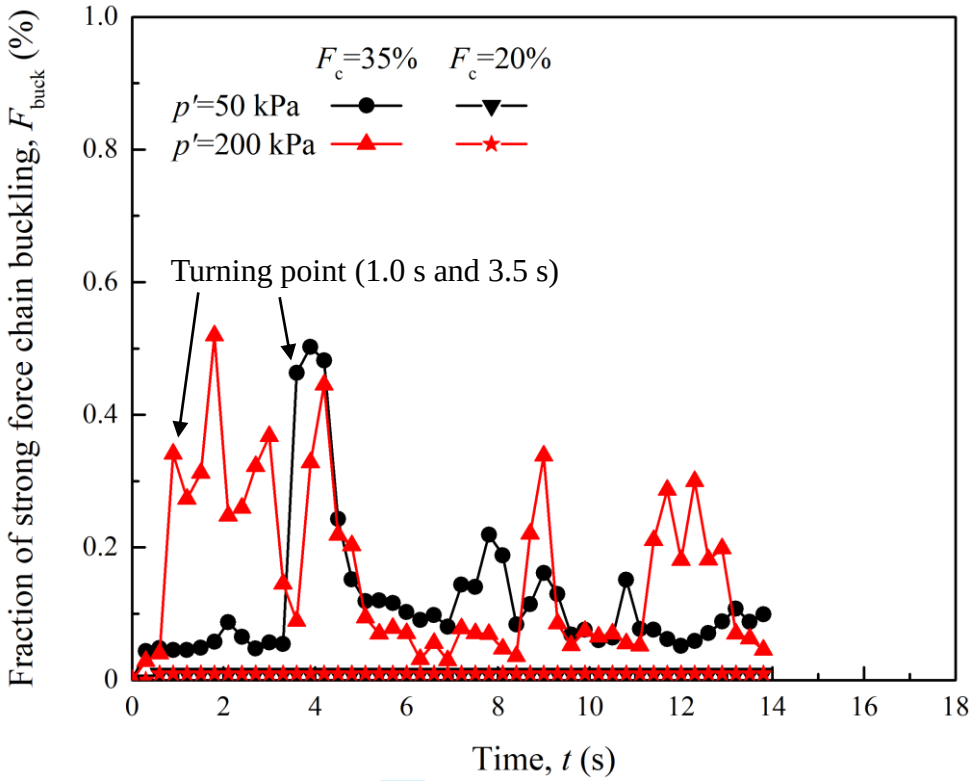

Figure 18 Fraction of strong force chain buckling for the samples with different F_c (20% and 35%) and p' (50 kPa and 200 kPa)

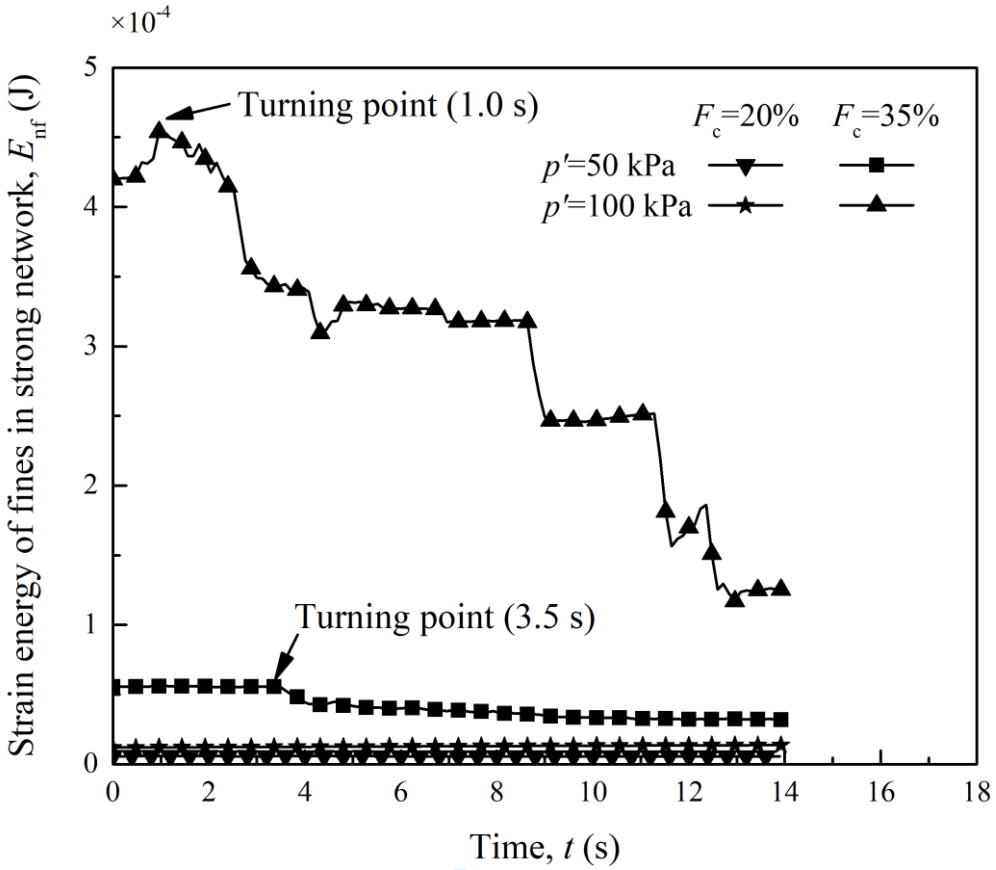

Figure 19 Strain energy of fines in strong network for the samples with different F_c (20% and 35%) and p' (50 kPa and 200 kPa)

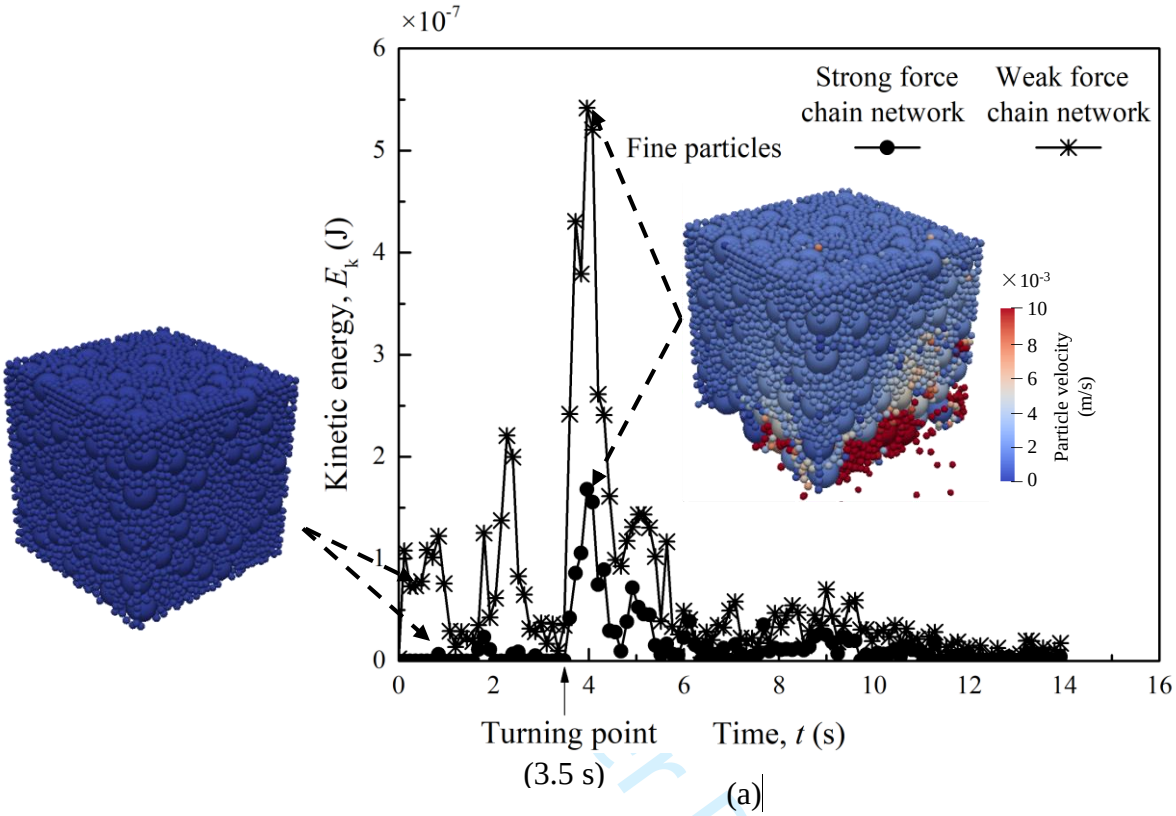
×10-7
Strong force chain network
Weak force chain network
Fine particles
Kinetic energy, Ek (J)
×10-3
Particle velocity (m/s)
Turning point (3.5 s)
Time, t (s)

(a)

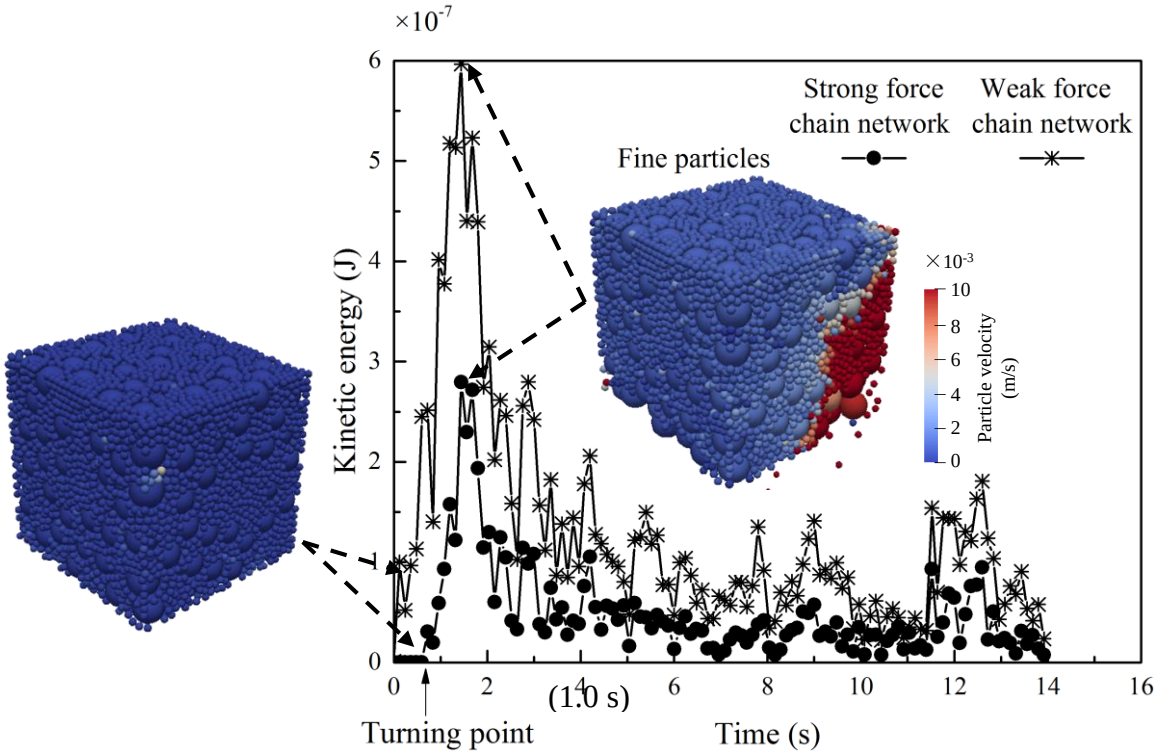
×10-7
Strong force chain network
Weak force chain network
Fine particles
Kinetic energy (J)
×10-3
Particle velocity (m/s)
Turning point (1.0 s)
Time (s)

(b)

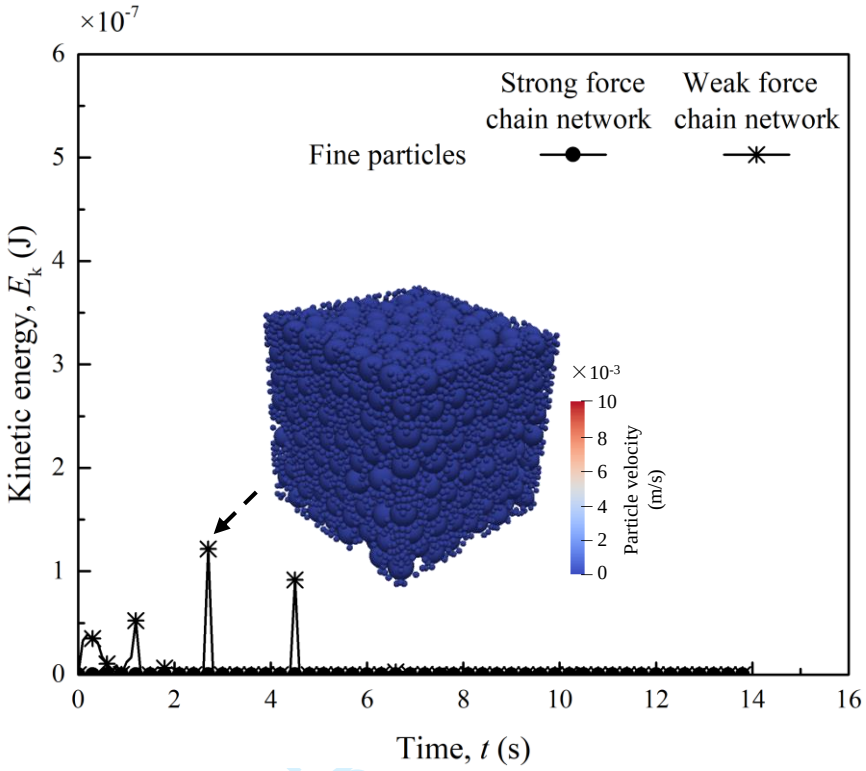

(c)

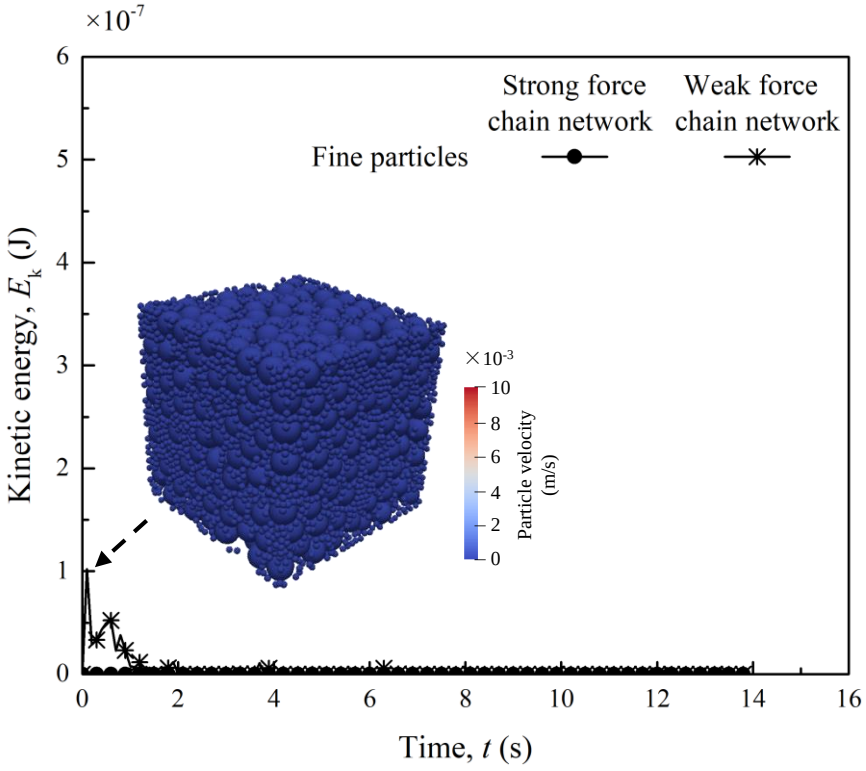

(d)

Figure 20 Kinetic energy of the fine particles in different networks for the samples with (a) F_c=35%, p'=50 kPa; (b) F_c=35%, p'=200 kPa; (c) F_c=20%, p'=50 kPa; (d) F_c=20%, p'=200 kPa

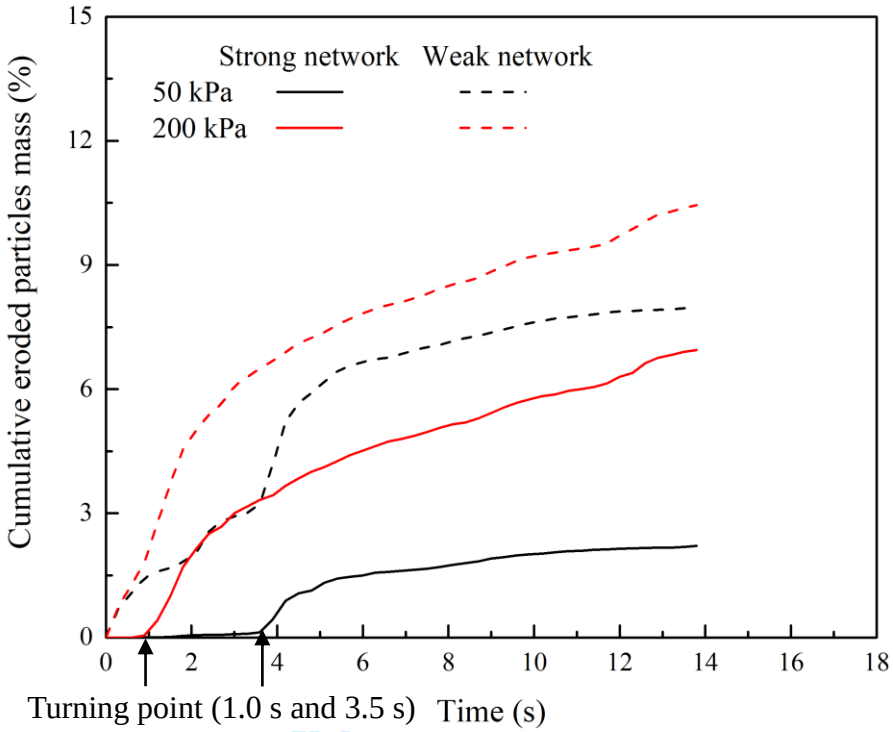

Figure 21 Cumulative eroded mass of fines in strong and weak networks